Microstructures and seismic properties of south Patagonian mantle xenoliths (Gobernador Gregores and Pali Aike)

Article *in* Tectonophysics · May 2014

DOI: 10.1016/j.tecto.2014.02.017

CITATIONS
12

READS
213

4 authors:

Claudia Zaffarana
CONICET-Universidad Nacional de Río Negro,…
14 PUBLICATIONS **147** CITATIONS
SEE PROFILE

Andréa Tommasi
Université de Montpellier
169 PUBLICATIONS **4,336** CITATIONS
SEE PROFILE

Alain Vauchez
Université de Montpellier
137 PUBLICATIONS **4,112** CITATIONS
SEE PROFILE

Michel Grégoire
Paul Sabatier University - Toulouse III
179 PUBLICATIONS **2,475** CITATIONS
SEE PROFILE

Tectonophysics xxx (2014) xxx–xxx

Contents lists available at ScienceDirect

Tectonophysics

journal homepage: www.elsevier.com/locate/tecto

Microstructures and seismic properties of south Patagonian mantle xenoliths (Gobernador Gregores and Pali Aike)

Claudia Zaffarana [a,b,*], Andréa Tommasi [a], Alain Vauchez [a], Michel Grégoire [c]

[a] Geosciences Montpellier, CNRS & Université Montpellier 2, F-34095 Montpellier, France
[b] Instituto de Geociencias Básicas, Aplicadas y Ambientales de Buenos Aires (I.G.E.B.A.), Consejo Nacional de Investigaciones Científicas y Técnicas (CONICET), Intendente Güiraldes 2160, C1428EGA, Ciudad Universitaria, Buenos Aires, Argentina
[c] Geosciences Environnement Toulouse, CNRS & Université de Toulouse, F-31400 Toulouse, France

ARTICLE INFO

Article history:
Received 14 October 2013
Received in revised form 8 February 2014
Accepted 22 February 2014
Available online xxxx

Keywords:
Subcontinental mantle lithosphere
Olivine
Orthopyroxene
Crystal preferred orientations
Annealing
Melt percolation

ABSTRACT

The subcontinental lithospheric mantle evolves through time due to tectonic events and processes as static recrystallization and melt percolation. To constrain the extent of these processes in the South Patagonian subcontinental mantle lithosphere we performed a microstructural and Electron Backscattered Diffraction (EBSD) study of a suite of 35 peridotite xenoliths brought to the surface by Plio-Pleistocene alkaline volcanic rocks from Gobernador Gregores and Pali Aike. All samples show a well-developed olivine and pyroxene crystallographic preferred orientation (CPO), consistent with deformation by dislocation creep with dominant activation of [100]{0kl} in olivine. The coarse granular or tabular textures and the low density of intracrystalline deformation features indicate that deformation was followed by annealing under static conditions. The xenoliths also show microstructural evidence of multiple episodes of reactive melt percolation. Neither annealing nor melt percolation erased the olivine CPO, which has [010]-fiber, [100]-fiber and orthorhombic patterns in Pali Aike xenoliths and essentially [010]-fiber and orthorhombic patterns in Gobernador Gregores xenoliths. Seismic properties calculated based on the CPO and modal compositions are, however, rather homogeneous, with fast S-wave polarization and P-wave propagation parallel to the [100] olivine axis. The variation in the olivine CPO solely changes the minimum S-wave birefringence direction, which is normal to the foliation for axial-[010] olivine CPO. Average samples for the two localities, obtained by adding up the individual samples CPO data in a common reference frame, show, however, a 'normal' upper mantle anisotropy with a maximum S-wave birrenfringence of ca. 5% at high angle to the both the maximum [010] and [100] axes concentrations, that is in the foliation, but normal to the lineation, and a minimum birefringence at low angle to the [100] maximum, that is parallel to the lineation.

1. Introduction

The formation and evolution of the subcontinental lithospheric mantle are still poorly understood. Seismic tomography and anisotropy allow probing its structure (Hess, 1964; Aki et al., 1977; Dziewonski et al., 1977), but the interpretation of these data in terms of thermal structure, compositional heterogeneity, and deformation history is not straightforward. Seismic velocity anomalies may result from both thermal heterogeneity and compositional heterogeneity. Anisotropy is directly related to the crystal preferred orientation (CPO) of olivine, which is produced by deformation in the upper mantle (e.g. Christensen, 1971; Mainprice, 2007; Nicolas and Christensen, 1987). The moderate temperatures that prevail in most of the lithospheric mantle allow the olivine CPO formed during major tectonic episodes to be preserved for very long time spans (e.g., Vauchez et al., 2005). However, are these CPO modified by processes such as heating leading to static recrystallization or melt percolation in the lithospheric mantle?

In this contribution, we studied the microstructures and CPO of olivine and pyroxenes in a collection of 35 mantle xenoliths from two volcanic localities in Southern Patagonia: Gobernador Gregores and Pali Aike (Fig. 1). These xenoliths sample the Patagonian mantle lithosphere, which underwent a complex geodynamic evolution in response to the various compressional and extensional events that affected its western and eastern margins. The analysis of the microstructures and CPO allowed partially deciphering the succession of deformation, thermal, and reactive melt percolation episodes that affected these peridotites. The modal composition, the olivine, orthopyroxene and clinopyroxene CPO data, and the equilibration temperatures and pressures from Dantas (2007) were used to calculate the seismic properties of these xenoliths and estimate the seismic anisotropy, composition and thermal state of the southern Patagonia mantle lithosphere in the vicinity of the two localities.

* Corresponding author. Tel./fax: +54 11 4788 3439.
E-mail address: cbzaffarana@gmail.com (C. Zaffarana).

http://dx.doi.org/10.1016/j.tecto.2014.02.017
0040-1951/

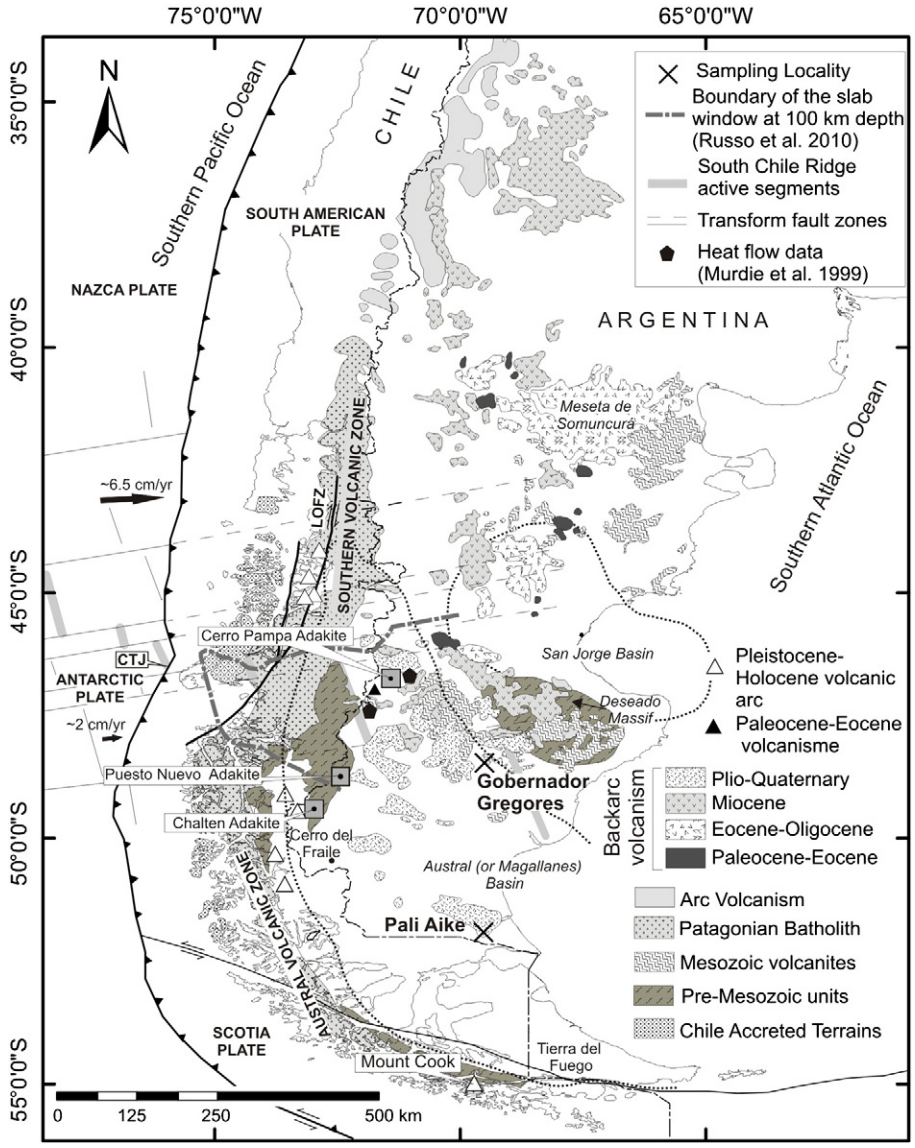

Fig. 1. Map showing the location of the xenolith-bearing localities relative to the main tectonic structures and geological units of Southern Patagonia. Modified from Ramos and Kay (1992), Kay et al. (1993), Lagabrielle et al. (2004), Ramos et al. (2004), Ramos (2008), Russo et al. (2010b), Castro et al. (2011). CTJ: Chile Triple Junction, LOFZ: Liquiñe–Ofqui Fault Zone.

2. Geodynamic setting

The southern Patagonia mantle lithosphere is at least as old as the late Proterozoic (Schilling et al., 2008). Late Proterozoic ages are also recorded in the crust. The Deseado Massif records rifting from Gondwana in the late Proterozoic to early Cambrian and re-accretion to it in the Carboniferous (Dalla Salda et al., 1992; Pankhurst et al., 2003, 2006, Fig. 1). In addition, ~530 Ma old orthogneisses were recovered from wells in northern Tierra de Fuego (Söllner et al., 2000).

More recently, two major geodynamic events affected the eastern and western margins of Patagonia: the opening of the South Atlantic and the Andean subduction, respectively. The breakup of Gondwana, which led to the opening of the South Atlantic during the Cretaceous, resulted in extension and voluminous rhyolitic volcanism in southern Patagonia ("Mesozoic volcanism" in Fig. 1, e.g., Pankhurst and Rapela, 1995; Pankhurst et al., 1998, 2000). Since then, the eastern margin of Patagonia has been dominated by subsidence and sedimentation, which formed the Austral (or Magallanes) basin (Fig. 1).

The eastward subduction along the western margin of Patagonia has been active since late Paleozoic times (e.g., Mpodozis and Ramos, 1989). This long-lived subduction has migrated and changed orientation through time (Mpodozis and Ramos, 2008; Rapela et al., 2005), attaining the present location (Fig. 1) in the late Jurassic (Breitsprecher and Thorkelson, 2009; Somoza and Ghidella, 2012). At ~14–15 Ma, the Chile ridge, which accommodates spreading between the Nazca and Antartic plates, collided with the trench forming the Chile Triple Junction (Cande and Leslie, 1986), which has since then migrated northward, being presently at 46.5° S (Fig. 1).

The Chile Triple Junction is characterized by a large negative Bouguer anomaly, interpreted as associated with upwelling of hot mantle in an asthenospheric window (Murdie, 1994; Murdie et al., 2000), and by a negative velocity anomaly relative to the surrounding asthenospheric mantle in both surface- and body-wave travel-time tomography models (Heintz et al., 2005; Russo et al., 2010b). Unusually warm asthenosphere below this region was also inferred from numerical modeling of post-glacial rebound information (Ivins and James, 1999) and from heat flow data (103 ± 15 mW m^{-2}; Murdie et al., 1999). Teleseismic shear wave splitting patterns also change in the vicinity of the Chile triple junction; fast polarization directions rotate from the general N–S direction to an ENE trend, suggesting that the mantle flow is diverted parallel to the subducted transform faults that are supposed to bound the slab window (Russo et al., 2010a,b).

Please cite this article as: Zaffarana, C., et al., Microstructures and seismic properties of south Patagonian mantle xenoliths (Gobernador Gregores and Pali Aike), Tectonophysics (2014), http://dx.doi.org/10.1016/j.tecto.2014.02.017

Since the Paleocene, the southern Patagonia was affected by an extensive alkaline volcanism that carried xenoliths from subcontinental mantle lithosphere to the surface ("Cenozoic volcanic rocks" in Fig. 1, e.g., Skewes and Stern, 1979; Stern et al., 1986, 1990; Gorring and Kay, 2001). The causes of this alkaline magmatism are still discussed. It has been proposed to be related to the ridge subduction, but its extension and age progression do not really fit this model. The volcanic fields where the xenoliths studied here have been sampled (Gobernador Gregores and Pali Aike, Fig. 1) belong to this magmatism. Gobernador Gregores is located at ~500 km SE of the present location of the Chile Triple Junction (Fig. 1). It is essentially composed by basaltic andesites and tholeitic basalts of Miocene age, but the xenoliths are carried by a post-plateau sequence composed by Plio-Pleistocene alkaline lavas and hawaiites (Gorring et al., 1997). The Pali Aike volcanic field is the southernmost among the patagonian plateau basalts, being located ~400 km south of Gobernador Gregores, ~750 km SE from the Chile Triple Junction, and ~400 km from the trench (Fig. 1). It extends over 4500 km^2 and is mainly (~80%) composed by basaltic lavas (D'Orazio et al., 2000). The xenoliths are born by post-plateau alkaline basalts and basanites of Pliocene to recent ages (3.8–0.2 Ma; Corbella, 1984, 2002; Linares and Gonzales, 1990; Mazzarini and D'Orazio, 2003).

Waveform inversion suggests that, away from the trench, southeastern Patagonia is characterized by low seismic velocities at asthenospheric depths, a lithospheric lid as thin as 65 km, and a crustal thickness of 26–34 km (Robertson Maurice et al., 2003). Such a thin lithospheric lid is, however, not consistent with thermobarometry data on Pali Aike xenoliths (Douglas et al., 1987; Skewes and Stern, 1979; Stern et al., 1986, 1989), which support a geothermal gradient >10 °C/km between 50 and 100 km depth leading to temperatures of ~1300 °C at 100 km depth, that is, a normal thickness for stable continental lithosphere.

3. Previous studies on Gobernador Gregores and Pali Aike mantle xenoliths

Geochemical studies of Gobernador Gregores and Pali Aike xenoliths have highlighted that the mantle beneath the two localities is extensively metasomatized, though the nature of the metasomatic fluids differs (Aliani et al., 2004; Bjerg et al., 2005; Dantas, 2007; Douglas et al., 1987; Gorring and Kay, 2000, 2001; Kempton et al., 1999a,b; Laurora et al., 2001; Rivalenti et al., 2004a,b; Skewes and Stern, 1979; Stern et al., 1986, 1989, 1999). REE data on clinopyroxenes from some of the peridotites analyzed in the present study (Fig. 2; Dantas, 2007) show that Cr-diopsides from Gobernador Gregores peridotites show variable LREE enrichment but flat Sm to Yb concentrations, positive Th and U spikes and negative Nb, Ta and Ti spikes. These results would suggest that the metasomatic agents in this locality are of alkaline composition (Dantas, 2007), in agreement with previous studies (Bjerg et al., 2005; Gorring and Kay, 2000; Laurora et al., 2001; Rivalenti et al., 2004b). Cr-diopsides from Pali Aike peridotites are more homogeneous, showing moderately depleted LREE and lithophile element compositions compatible with metasomatic agents of tholeitic composition (Fig. 2; Dantas, 2007). These results are compatible with the studies of Stern et al. (1986, 1989), which signaled that the peridotites of Pali Aike have trace-element and isotopic compositions consistent with a depleted mantle (MORB-producing) source which has been modified by interaction with slab-related fluids or melts (Stern et al., 1986, 1989) or with melts similar to the host basalt (Kempton et al., 1999a).

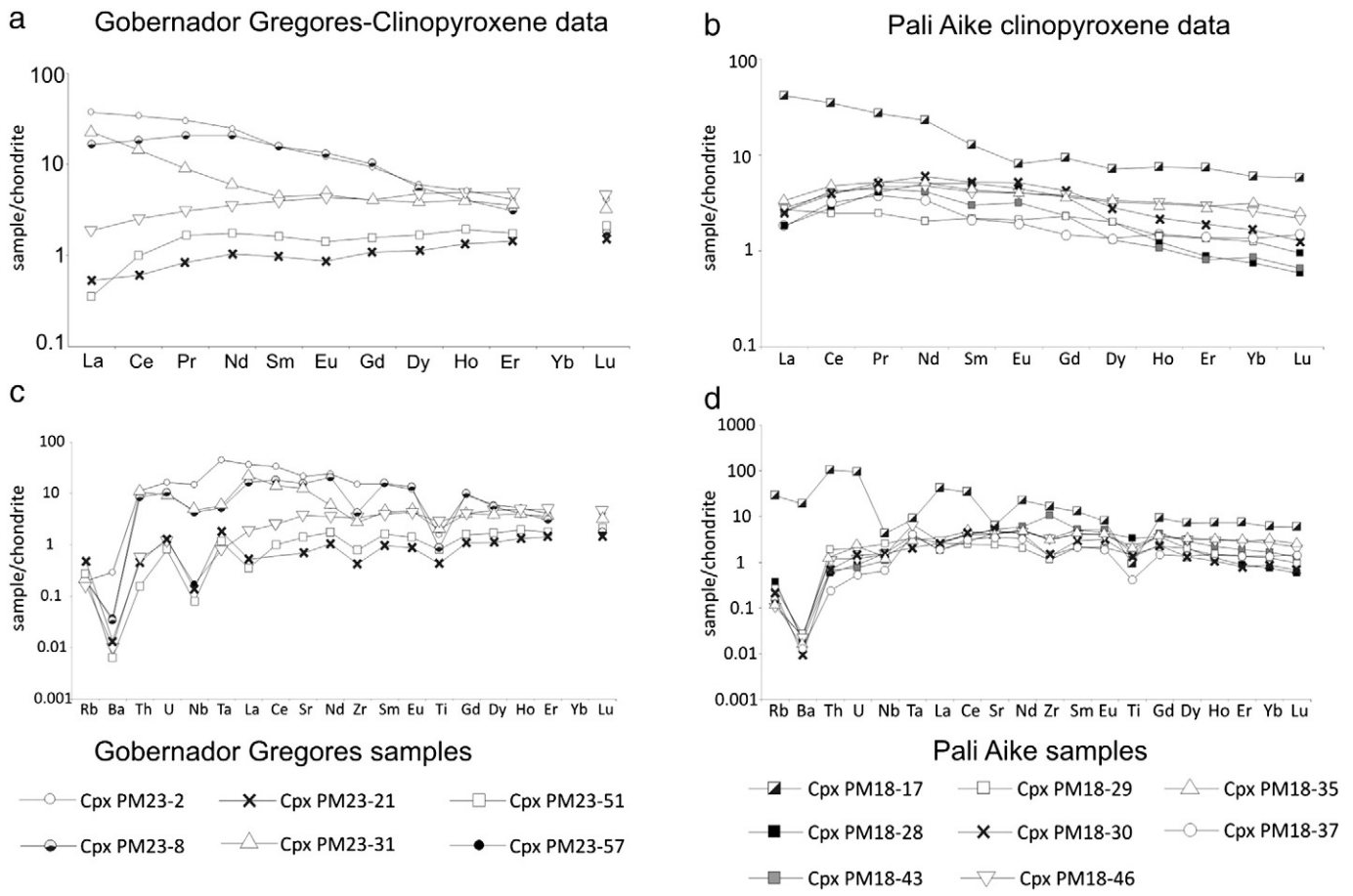

Fig. 2. Chondrite normalized (McDonough and Sun, 1995) REE (a–b) and extended trace element (c–d) contents in clinopyroxenes from Gobernador Gregores peridotites (a,c) and Pali Aike peridotites (b–c) (from Dantas, 2007).

Please cite this article as: Zaffarana, C., et al., Microstructures and seismic properties of south Patagonian mantle xenoliths (Gobernador Gregores and Pali Aike), Tectonophysics (2014), http://dx.doi.org/10.1016/j.tecto.2014.02.017

Thermobarometry studies on Pali Aike garnet and spinel peridotites and garnet peridotite evidence equilibrium pressure and temperature (PT) conditions ranging from ~960 °C/1.8 GPa to 1160 °C/2.4 GPa (Bjerg et al., 2005; Douglas et al., 1987; Skewes and Stern, 1979; Stern et al., 1986, 1989). These data align on a geotherm with a gradient of ~10 °C/km in the mantle lithosphere that crosscuts the 1250 °C adiabat at ~95 km depth (Fig. 3). Equilibrium PT conditions obtained by Dantas (2007) using the opx-cpx thermometer and the gt-opx barometer of Brey and Köhler (1990) for 9 garnet and spinel peridotites analyzed in the present study (Table 1) fall along this geotherm, with exception of a phlogopite-bearing garnet and spinel lherzolite, which seems to have equilibrated on a cooler geotherm (Fig. 3). However, pyroxenes in this sample are suspected not to be in equilibrium (Dantas, 2007). The equilibrium temperature of 990 °C (BK90) and pressure of 2.15 GPa displayed by the amphibole-bearing garnet and spinel lherzolite are well into the pargasite stability field for moderate to high water contents (Green et al., 2010).

Equilibrium temperatures for anhydrous spinel lherzolites of Pali Aike range from 1018 to 1052 °C (Table 1, Dantas, 2007) and if they are placed in the same geotherm than the garnet and spinel lherzolites they would have been equilibrated at similar pressures (1.9 to 2.2 GPa, Fig. 3). This apparent contradiction could be explained if the spinel lherzolites were richer in Cr, as this displaces the spinel to garnet transition to higher pressures (Klemme, 2004), but both rocks have aluminous spinels (Cr# = 20–29, Dantas, 2007). The similar equilibrium temperatures obtained for spinel peridotites and garnet and spinel lherzolites suggest therefore that the thermal state of the lithosphere beneath Pali Aike may not follow a simple stationary geotherm. Indeed, core-to-rim chemical zonation of orthopyroxenes in xenoliths equilibrated at temperatures >900 °C indicates that these xenoliths experienced a heating event (Stern et al., 1999). Heating (or decompression) is also suggested by the kelyphitic rims developed by some of the high-T garnet peridotites (Stern et al., 1999).

Gobernador Gregores xenoliths are all spinel facies peridotites. Equilibration temperatures obtained by Dantas (2007) using the geothermometer of Brey and Köhler (1990) on 5 of the peridotites analyzed on the present study range between 713 and 1054 °C (Table 1, Dantas, 2007). The fertile compositions of these xenoliths (Table 1) and aluminous nature of the spinels (average Cr# = 29, Dantas, 2007) suggest that these xenoliths equilibrated at depths <70 km. If the equilibration temperatures obtained by Dantas (2007) are plotted on the Pali Aike geotherm, the spinel peridotites of Gobernador Gregores would have equilibrated between 35 and 70 km depth (Fig. 3). On the other hand, if the much higher surface heat flow of ca. 100 mW/m^2 measured by Murdie et al. (1999) in the lakes General Carrera and Cochrane in Chile (Fig. 1) is considered, Gobernador Gregores xenoliths would derive from depths shallower than 30 km (Fig. 3), which is not consistent with the Moho depths >30 km defined seismologically (Lawrence and Wiens, 2004; Robertson Maurice et al., 2003).

4. Methods

Microstructures were characterized by optical analysis of polished thin sections cut in a random orientation, because the foliation and lineation could not be determined in most macroscopic samples. Olivine and pyroxene crystal preferred orientations (CPO) were determined at Geosciences Montpellier using a JEOL 5600 scanning electron microscope equipped with an EBSD system from Oxford HKL Technology. Automatic orientation mapping with step sizes ranging from 30 to 100 μm, depending on the average grain size, was carried out over the entire thin sections (in most cases ~30 × 25 mm area has been analyzed). An accelerating voltage of 17 kV and a 25 mm working distance were used.

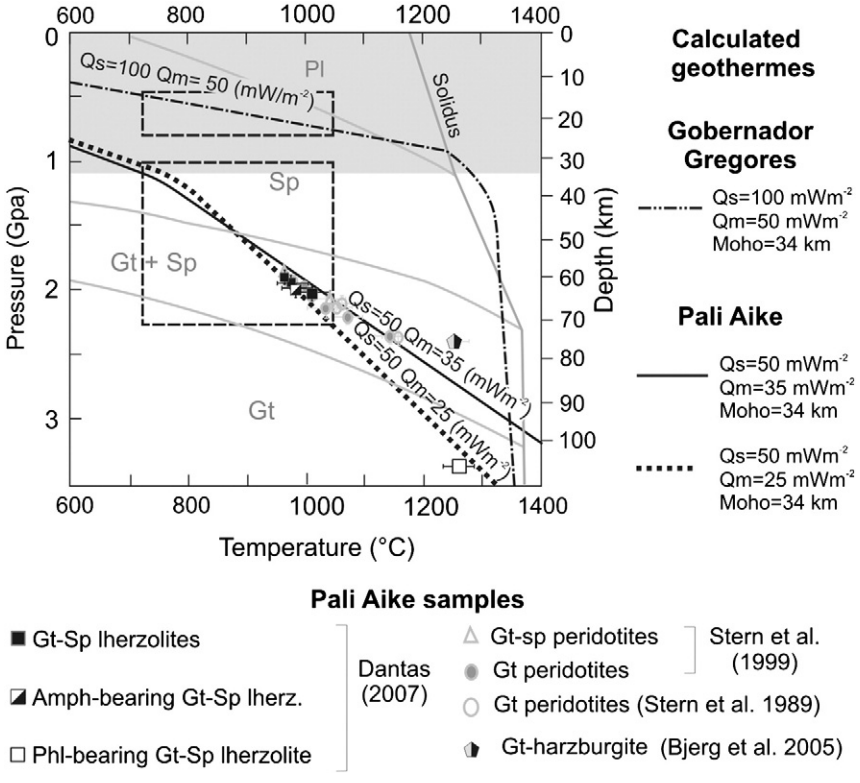

Fig. 3. Equilibration pressure and temperature data for Pali Aike xenoliths compiled from Stern et al. (1989, 1999), Bjerg et al. (2005), and Dantas (2007). Calculated steady-state geotherms obtained considering a 34 km thick crust (in gray) and the surface (Qs) and reduced heat flows (Qm) given on the side of each curve are shown for comparison. The hotter geotherm is consistent with the surface heat flow of ca. 100 mW/m^2 measured by Murdie et al. (1999). The boxes indicate possible provenance depths of Gobernador Gregores spinel peridotites if the equilibration temperatures from Dantas (2007) are projected on these geotherms. Phase diagrams for a fertile mantle are also shown (modified from Green and Ringwood, 1967; Irving, 1974; Ringwood, 1975; Obata, 1976; Presnall, 1976; Herzberg, 1978; Perkins et al., 1981; Gasparik, 1984; Wood and Holloway, 1984; Kornprobst, 1970; Klemme and O'Neill, 2000; Klemme, 2004). Error bars for temperature and pressure data are ±50 °C and ±0.1 GPa, respectively (Brey and Köhler, 1990). Gt: garnet, Sp: spinel, Pl: plagioclase.

Please cite this article as: Zaffarana, C., et al., Microstructures and seismic properties of south Patagonian mantle xenoliths (Gobernador Gregores and Pali Aike), Tectonophysics (2014), http://dx.doi.org/10.1016/j.tecto.2014.02.017

Table 1
Locality, sample number, rock type, modal composition, and geothermobarometric data from Dantas (2007). Equilibration temperatures (T-BK90) and pressures were obtained using the opx-cpx geothermomether and opx-gt geobarometer of Brey and Köhler (1990). For the spinel peridotites, temperature was calculated using a fixed pressure of 1.5 GPa.

Locality	Sample #	Rock type	Modal composition (EBSD mapping + observation)							P,T equilibration conditions	
			Ol	Opx	Cpx	Gt	Sp	Phl	Amph	Cpx /Opx	T-BK90 (°C)	P (GPa)
GG	PM23-26	Sp lherzolite	87	8	5	0	0	0	0	0.63	–	–
GG	PM23-36	Sp lherzolite	68	24	7	0	1	0	0	0.29	–	–
GG	PM23-51	Sp lherzolite	72	19	7	0	2	0	0	0.37	779	–
GG	PM23-52	Sp lherzolite	73	18	7	0	2	0	0	0.39	–	–
GG	PM23-31	Sp lherzolite	78	14	7	0	1	0	0	0.50	1054	–
GG	PM23-57	Sp lherzolite	68	21	7	0	4	0	0	0.33	841	–
GG	PM23-21	Sp lherzolite	70	19	10	0	1	0	0	0.53	713	–
GG	PM23-38	Sp lherzolite	79	7	13	0	1	0	0	1.86	–	–
GG	PM23-46	Amph-bearing Sp harzburgite	72	19	3.5	0	0.5	0	5	0.18	–	–
GG	PM23-54	Amph-bearing Sp lherzolite	71	20	5	0	0	0	4	0.25	–	–
GG	PM23-12	Amph-bearing Sp lherzolite	70	20	7	0	0	0	3	0.35	–	–
GG	PM23-48	Sp dunite with websteritic veins	60	10	30	0	0	0	0	0.30	–	–
GG	GG22	Amph-bearing wehrlite	85	0	10	0	0	0	5	–	–	–
GG	PM23-8	Amph-bearing wehrlite	56	0	33	0	0	0	11	–	–	–
GG	PM23-2	Phl-bearing Sp lherzolite	83	5	9	0	1	2	0	1.80	1051	–
PA	PM18-22	Gt-Sp lherzolite	57	35	5	2.9	0.1	0	0	0.14	–	–
PA	PM18-20	Gt-Sp lherzolite	60	30	6	3	1	0	0	0.20	–	–
PA	PM18-42	Gt-Sp lherzolite	65	20	12	2	1	0	0	0.60	–	–
PA	PM18-29	Gt-Sp lherzolite	62	20	13	4	1	0	0	0.65	998	2.08
PA	PM18-46	Gt-Sp lherzolite	65	16	15	3	1	0	0	0.94	994	1.8
PA	PM18-8	Gt-Sp lherzolite	63	16	15	5	1	0	0	0.94	–	–
PA	PM18-28	Gt-Sp lherzolite	58	21	15	5	1	0	0	0.71	1076–1232	2.35
PA	PM18-30	Gt-Sp lherzolite	63	15	16	5	1	0	0	1.07	1017	1.91
PA	PM18-21	Gt-Sp lherzolite	55	22	17	5	1	0	0	0.77	–	–
PA	PM18-12	Gt-Sp lherzolite	60	12	20	6	2	0	0	1.67	–	–
PA	PM18-7	Gt-Sp lherzolite	54	22	20	3	1	0	0	0.91	–	–
PA	PM18-39	Gt-Sp lherzolite	53	20	22	4.5	0.5	0	0	1.10	–	–
PA	PM18-17	Amph-bearing Gt-Sp lherz.	50	34.5	9	5	0.5	0	1	0.26	990	2.15–2.18
PA	PM18-5	Amph-bearing Gt-Sp lherz.	68	18	9.5	2	0.5	0	2	0.53	–	–
PA	PM18-24	Phl-bearing Gt-Sp lherzolite	55	37	5	2	0.5	0.5	0	0.14	1257	3.4
PA	PM18-43	Sp lherzolite	64	30.5	5	0	0.5	0	0	0.16	1052	–
PA	PM18-26	Sp lherzolite	75	15	8	0	2	0	0	0.53	–	–
PA	PM18-37	Sp lherzolite	66	24.5	9	0	0.5	0	0	0.37	1023	–
PA	PM18-35	Sp lherzolite	62	26	11	0	1	0	0	0.42	1018	–
PA	PM18-27	Amph-bearing Sp lherzolite	68	17	13	0	1	0	1	0.76	–	–

Indexation rates ranged from 60 to 90%. Post-acquisition data treatment performed with the Tango software (HKL-Oxford Instruments) allowed to further increase the indexation rate by 1) filling the non-indexed pixels that have up to 8 identical neighbors with the same orientation 2) repeating this operation iteratively for 7, 6, and 5 identical neighbors, and 3) correcting the systematic olivine indexation errors due to olivine hexagonal pseudo-symmetry, which results in similar diffraction patterns for orientations differing by a rotation of 60° around [100]. The resulting orientation maps were verified after each correction step in order to avoid over-extrapolation of the data.

Crystallographic preferred orientation data are displayed as pole figures, presented as lower hemisphere stereographic projections. To avoid over-representation of large grains, data were plotted as one point per grain. To allow easy comparison among different samples, we rotated all CPO into a common orientation, in which the maximum concentration of olivine [100] axis was placed in the E–W direction and the maximum concentration of the [010] axis was placed in the N–S direction of the pole figure. This choice is justified by the concentration of [010] axes of olivine normal to the crystals elongation in the samples with an olivine shape preferred orientation (cf. Section 6. Microstructures and Table 2). In addition, parallelism of the X structural direction (lineation) with the maximum concentration of [100] olivine is corroborated by: (1) the stronger concentration of [100] relative to [001], as numerical simulations of CPO evolution show that the dominant slip direction concentrates faster (Tommasi et al., 2000; Wenk et al., 1991) and (2) its parallelism to the orientation of the [001] maximum of the pyroxenes when it was contained in the foliation plane, as pyroxenes display a single dominant slip direction, which is [001].

The strength of CPO is represented by the J index, a dimensionless fabric strength index obtained by the integration of the squared density of the orientation distribution function (ODF) over the entire volume: $J = \int f(g)^2 dg$, where f(g) is the orientation distribution function and dg is $dg = d\varphi 1 d\Phi d\varphi 2 \sin\Phi/\pi^2$, where φ1, φ, and φ2 are the Euler angles that define the rotations allowing for coincidence between the crystallographic and external reference frames (Bunge, 1982). For a random distribution J = 1 and for a single crystal J is infinite. The J index of olivine has been calculated using the texture analysis software MTEX (Hielscher and Schaeben, 2008; Bachmann et al., 2010; Mainprice et al., 2011; http://mtex.googlecode.com). Further analysis of the olivine crystal preferred orientation symmetry was performed using the point (P), girdle (G) and random (R) fabric type indices for the olivine [100], [010] and [001] distributions. These indices are calculated from the three eigenvalues ($lambda_1$, $lambda_2$, $lambda_3$) of the normalized orientation matrix for each principal crystallographic axes as: $P = \lambda_1 - \lambda_3$, $G = 2(\lambda_2 - \lambda_3)$ and $R = 3\lambda_3$ (Vollmer, 1990). These indices may be combined for a more throughout analysis of the symmetry of the CPO. The BA index, defined as $BA = 0.5 * (2.0 - (P_{010} / (G_{010} + P_{010})) - (G_{100} / (G_{100} + P_{100})))$ is used here, for instance, for quantifying the tendency of the olivine CPO towards end-member fiber-[010] (BA = 0) or fiber-[100] patterns (BA = 1).

In samples where the thin section was cut close to the XZ plane, that is where the thin section plane contained both the olivine [100] and [010] maximum concentrations, grain sizes and shape preferred orientation were determined from the EBSD maps using the automatic grain detection routine in the MTEX software (http://mtex.googlecode.com). This approach is based on a Voronoi decomposition and fills

Please cite this article as: Zaffarana, C., et al., Microstructures and seismic properties of south Patagonian mantle xenoliths (Gobernador Gregores and Pali Aike), Tectonophysics (2014), http://dx.doi.org/10.1016/j.tecto.2014.02.017

Table 2
Texture, fabric strength (J index calculated using one orientation datum per grain), olivine CPO symmetry characterized by the BA index, correlation between olivine and pyroxene's CPO, average density (measured at room temperature and pressure conditions) and seismic properties: AVp = maximum propagation anisotropy of P-waves, AVs_1 = maximum propagation anisotropy of S_1-waves, AVs_2 = maximum propagation anisotropy of S_2-waves, AVs_{max} = maximum S-wave polarization anisotropy for all studied samples.

Locality	Sample	Rock type	Main microtextural characteristics	J index	BA Index	Olivine CPO type	[100] Olivine // [001] pyroxene(s)?	Average density (g/cm^3)	Seismic properties			
									AVp (%)	AVs_{1max} (%)	AVs_{2max} (%)	AVs_{max} (%)
GG	PM 23-26	Sp lherzolite	Coarse granular — polygonal	9.28	0.74580	Fiber-[100]	Yes	3.3488	16.29	6.2835	8.0886	10.65
GG	PM 23-36	Sp lherzolite	Coarse granular — polygonal	6.50	0.82170	Fiber-[100]	Yes	3.3393	12.66	4.1623	7.1239	8.47
GG	PM 23-51	Sp lherzolite	Coarse granular — polygonal	4.78	0.91090	Fiber-[100]	Yes	3.3406	11.88	4.5764	6.3941	7.88
GG	PM 23-52	Sp lherzolite	Coarse granular — polygonal	6.04	0.69990	Fiber-[100]	No	3.3453	12.69	4.8961	5.8471	8.02
GG	PM 23-31	Sp lherzolite	Granular?, olivine SPO, but no well-developed crystallographic faces	4.20	0.55720	Orthorhombic	No	3.3452	9.27	2.8243	5.1235	6.26
GG	PM 23-57	Sp lherzolite	Coarse granular	7.76	0.63920	Fiber-[100]	No	3.3423	12.60	4.5841	6.8399	8.47
GG	PM 23-21	Sp lherzolite	Coarse granular — polygonal with some tabular crystals	3.71	0.43990	Orthorhombic	Yes	3.3386	8.29	3.7871	4.2528	6.07
GG	PM 23-38	Sp lherzolite	Coarse granular	4.74	0.76660	Fiber-[100]	Yes	3.3423	11.39	3.2757	5.8604	6.84
GG	PM 23-46	Amph-bearing Sp harzb.	Coarse granular — polygonal	4.29	0.57030	Orthorhombic	No	3.3325	6.30	2.1163	3.5586	4.28
GG	PM 23-54	Amph-bearing Sp lherz.	Coarse granular — polygonal	4.27	0.41330	Orthorhombic	Yes	3.3331	7.07	3.6055	3.9794	5.44
GG	PM 23-12	Amph-bearing Sp lherz.	Coarse granular — polygonal	4.96	0.54370	Orthorhombic	Yes	3.3376	10.14	4.5609	4.436	6.30
GG	PM 23-48	Sp dunite with websteritic veins	Coarse granular, but veins produce a secondary tabular microstructure	4.20	0.68390	Fiber-[100]	-	3.3308	9.52	2.5258	5.4351	6.41
GG	GG22	Amph-bearing wehrlite	Tabular	3.56	0.49770	Orthorhombic	Yes	3.3441	5.83	3.2343	3.7136	5.28
GG	PM 23-8	Amph-bearing wehrlite	Coarse granular — sutured grain boundaries	3.33	0.41780	Orthorhombic	Yes	3.3107	6.06	3.7412	3.6503	4.96
GG	PM 23-2	Phl-bearing Sp lherzolite	Tabular	3.66	0.30750	Fiber-[010]	No	3.334	9.14	3.7412	3.6503	6.27
PA	PM 18-22	Gt-Sp lherzolite	Granular, with an olivine SPO but no well-developed crystallographic faces	3.40	0.61270	Orthorhombic	Yes	3.3417	4.65	2.7988	2.6045	3.67
PA	PM 18-20	Gt-Sp lherzolite	Granular	3.31	0.38860	Fiber-[010]	Yes	3.3438	8.10	3.5907	3.8938	5.90
PA	PM 18-42	Gt-Sp lherzolite	Granular	5.64	0.52780	Orthorhombic	No	3.3416	6.47	2.2916	3.3844	3.96
PA	PM 18-29	Gt-Sp lherzolite	Granular polygonal with tabular tendency	3.81	0.28690	Fiber-[010]	Yes	3.3434	8.24	4.7135	3.3516	6.07
PA	PM 18-46	Gt-Sp lherzolite	Granular polygonal with tabular tendency	2.17	0.79380	Fiber-[100]	No	3.3449	5.88	1.8241	3.1695	3.81
PA	PM 18-8	Gt-Sp lherzolite	Granular — polygonal	3.04	0.54270	Orthorhombic	Yes	3.3452	6.04	2.8759	2.6174	4.44
PA	PM18-28	Gt-Sp lherzolite	Granular?, olivine SPO, but no well-developed crystallographic faces	2.68	0.19980	Fiber-[010]	Yes	3.3452	4.93	3.5353	1.4867	3.81
PA	PM 18-30	Gt-Sp lherzolite	Granular — polygonal	2.83	0.60320	Orthorhombic	No	3.3428	5.34	2.7883	2.6406	4.07
PA	PM 18-21	Gt-Sp lherzolite	Granular polygonal with tabular tendency	3.04	0.32260	Fiber-[010]	No	3.3469	6.48	3.1045	2.4864	4.87
PA	PM 18-12	Gt-Sp lherzolite	Granular polygonal with tabular tendency	3.18	0.33130	Fiber-[010]	Yes	3.3449	6.16	3.4191	1.6088	4.36
PA	PM 18-7	Gt-Sp lherzolite	Granular — polygonal	2.76	0.60470	Fiber-[100]	No	3.3347	5.93	2.605	3.3773	4.23
PA	PM 18-39	Gt-Sp lherzolite	Granular polygonal with tabular tendency	3.61	0.68290	Fiber-[100]	No	3.3467	8.03	2.4414	4.3547	4.95
PA	PM 18-17	Amph-bearing Gt-Sp lherz.	Granular — polygonal	2.79	0.74950	Fiber-[100]	Yes	3.343	5.53	1.5613	3.7523	4.28
PA	PM 18-5	Amph-bearing Gt-Sp lherz.	Granular polygonal with tabular tendency	2.64	0.37780	Fiber-[010]	No	3.3399	5.78	2.4263	2.9103	4.07
PA	PM 18-24	Phl-bearing Gt-Sp lherz.	Primary microstructure obscured by secondary (reactional) crystallization	5.99	0.30600	Fiber-[010]	No	3.3399	5.78	3.0739	2.703	4.07
PA	PM 18-43	Sp lherzolite	Granular?, olivine SPO, but no well-developed crystallographic faces	3.44	0.80880	Fiber-[100]	Yes	3.337	7.08	2.1731	4.0853	4.52
PA	PM 18-26	Sp lherzolite	Granular polygonal with tabular tendency	3.01	0.61790	Fiber-[100]	No	3.3425	7.06	3.2146	3.8947	5.45
PA	PM 18-37	Sp lherzolite	Granular polygonal with strong tabular tendency	4.09	0.24930	Fiber-[010]	No	3.3365	8.31	4.7201	2.1971	5.75
PA	PM 18-35	Sp lherzolite	Granular — polygonal	4.05	0.74480	Fiber-[100]	No	3.3347	7.88	2.1857	4.6231	2.19
PA	PM 18-27	Amph-bearing Sp lherzolite	Granular?, olivine SPO, but no well-developed crystallographic faces	3.54	0.55980	Orthorhombic	No	3.3369	6.61	2.3098	3.6784	5.15

Please cite this article as: Zaffarana, C., et al., Microstructures and seismic properties of south Patagonian mantle xenoliths (Gobernador Gregores and Pali Aike), Tectonophysics (2014), http://dx.doi.org/10.1016/j.tecto.2014.02.017

missing measurements in a consistent, phase and rotational invariant way (Bachmann et al., 2011).

Seismic properties were estimated by averaging the elastic constants of olivine, orthopyroxene, clinopyroxene, amphibole, phlogopite, and garnet as function of their modal proportions and crystallographic orientations and solving the Christoffel equation (Mainprice, 1990, 2007; Mainprice and Humbert, 1994). Spinel, which occurs in small proportions (<5%) in all specimens (Table 1), was not considered. Seismic properties were calculated for ambient pressure and temperature conditions using the MTEX software (Mainprice et al., 2011). We used experimentally determined elastic constants for the olivine, orthopyroxene, clinopyroxene, garnet, amphibole and phlogopite single crystals (Abramson et al., 1997; Alexandrov and Ryzhova, 1961; Alexandrov et al., 1966; Chai et al., 1997; Collins and Brown, 1998; Duffy and Vaughan, 1988) and a Voigt–Reuss–Hill averaging scheme. Modal compositions were derived from the EBSD maps.

5. Modal compositions

Gobernador Gregores samples are all spinel peridotites, comprising eight spinel lherzolites, three amphibole-bearing spinel peridotites (two lherzolites and one harzburgite), two amphibole-bearing wehrlites, one dunite crosscut by clinopyroxenite veins with orthopyroxene-rich reaction walls, and one phlogopite-bearing spinel lherzolite (Fig. 4a and Table 1). The studied dataset is representative of the main lithologies present in Gobernador Gregores (Laurora et al., 2001; Rivalenti et al., 2004a,b). The spinel lherzolites of Gobernador Gregores have an average composition of ~74% olivine, ~16% orthopyroxene, ~8% clinopyroxene, and ~2% spinel, which is consistent with a partial melting trend. However, many Gobernador Gregores xenoliths display marked enrichments in clinopyroxene and/or olivine relative to a partial melting trend, indicating reaction with percolating melts (Fig. 4b). The end-member products of this melt–rock reaction are the wehrlites and dunites. A clear evidence for late-stage reactive melt percolation in this suite is the websteritic veins (clinopyroxenite veins with orthopyroxene-rich reaction rims) that crosscut the dunite. Modal metasomatism in this xenolith suite is also expressed by the crystallization of hydrous minerals. Amphibole content may reach up to 5% in the amphibole-bearing spinel lherzolites or harzburgites and 11% in the amphibole-bearing wehrlites (Table 1). High amphibole contents also characterize the clinopyroxenite veins in the dunite. Phlogopite content in the phlogopite-bearing spinel lherzolite is 2% (Table 1).

Pali Aike xenoliths either contain garnet and spinel or only spinel. They comprise 14 garnet and spinel lherzolites, among which 2 contain amphibole, one phlogopite-bearing garnet and spinel lherzolite, and 5 spinel lherzolites, among which one contains amphibole (Fig. 4a, Table 1). This dataset is representative of the range in lithologies usually sampled by Pali Aike xenoliths (Stern et al., 1999). The average composition of the studied Pali Aike xenoliths is more fertile than the Gobernador Gregores' one (~60% olivine, ~20% orthopyroxene, ~15% clinopyroxene, ~4% garnet, ~1% spinel, Table 1). Although extreme compositions, like wehrlites or dunites, are not present at Pali Aike, modal compositions often differ significantly from typical partial melting trends; most samples show enrichment in either ortho- or clinopyroxene, suggesting reactive melt percolation leading to refertilisation (Fig. 4b). Modal contents of hydrous minerals are lower in Pali Aike relative to Gobernador Gregores xenoliths: amphibole and phlogopite contents are ≤2% and 0.5%, respectively (Table 1).

6. Microstructures

All studied xenoliths, regardless of their modal composition, are medium to coarse-grained (grain sizes range from ~1 to ~10 mm). Gobernador Gregores peridotites are in average coarser grained than Pali Aike peridotites, but the microstructures of the xenoliths from the two sites are very similar. Peridotites from both sites present dominantly granular microstructures characterized by roughly equidimensional olivine crystals with dominantly polygonal grain boundaries forming 120° triple junctions (Fig. 5a). Some lherzolites have elongated olivines (with aspect ratios that may reach 5:1) showing a clear olivine shape preferred orientation. These elongated olivine crystals may display well-developed crystal faces, giving rise to a tabular microstructure (Fig. 5b), or curved grain boundaries (Fig. 5c). Intermediate microstructures between granular and tabular (Fig. 5d) are also commonly observed, in particular among Pali Aike xenoliths. A summary of the most important microstructural features of each sample is given in Table 2.

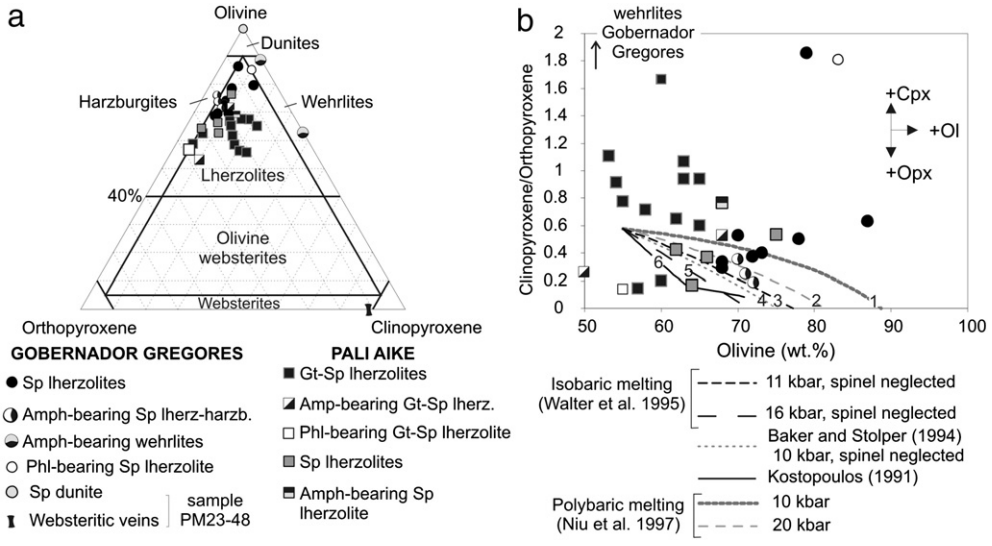

Fig. 4. (a) Modal compositions of the studied peridotites plotted onto the olivine–orthopyroxene–clinopyroxene diagram. Modes were obtained from the EBSD maps and confirmed by optical microscopy analysis of the thin sections. (b) Clinopyroxene/orthopyroxene ratio as a function of the olivine content. Modal compositions were recalculated for an olivine–opx-cpx system for comparison with melting models: (1) and (2) polybaric melting at starting at 1 and 2 GPa respectively (Niu et al., 1997), (3) and (4) isobaric melting at 1.1 GPa and 1.6 GPa (Walter et al., 1995) for an initial modal composition of 55% olivine, 28% opx, 15% cpx, and 2% spinel. The same symbols represent the sample compositions in panels (a) and (b).

Please cite this article as: Zaffarana, C., et al., Microstructures and seismic properties of south Patagonian mantle xenoliths (Gobernador Gregores and Pali Aike), Tectonophysics (2014), http://dx.doi.org/10.1016/j.tecto.2014.02.017

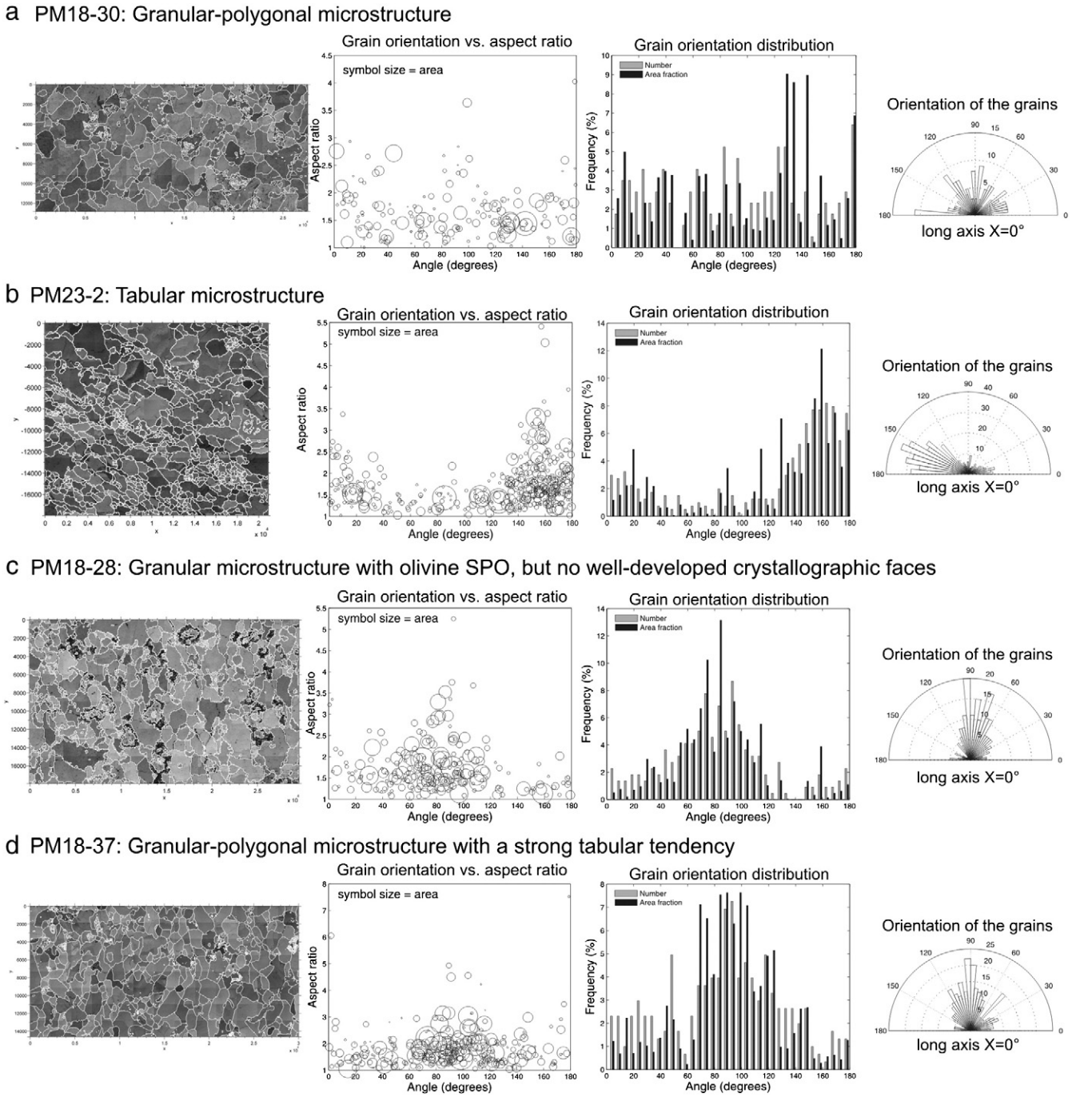

Fig. 5. Shape preferred orientation (SPO) data from samples with granular-polygonal microtexture (a), with tabular microstructure (b) and with microstructure intermediate between granular and tabular (c and d). From left to right: band contrast EBSD map with grain boundaries (misorientations ≥ 15°) highlighted in white, grain orientation vs. aspect ratio scatter diagram (symbols size are a function of the grain area), and the grains' orientation displayed as a histogram and a rose diagram (in both 0° corresponds to the +X direction).

Fig. 6. Typical microstructures of Gobernador Gregores peridotites. Left column: photomicrographs in cross-polarized light, right column: modal composition and grain boundary maps; olivine is shown in white, pyroxenes in gray (orthopyroxene: dark gray, clinopyroxene: light gray), spinel in yellow, hydrated phases (either amphibole or phlogopite) in light blue, non-indexed points in black. Grain boundaries (misorientations angles > 15°) are shown in black, subgrain boundaries (misorientations between 2 and 15°) are marked in red. (a–b) Coarse-grained amphibole-bearing spinel lherzolite PM23-12 with sutured to polygonal olivine–olivine grain boundaries; clinopyroxene bears concave grain boundaries towards olivine and amphibole crystals show olivine inclusions. (c–d) Medium- to coarse-grained spinel lherzolite PM23-52 with polygonal texture. (e–f) Medium-grained phlogopite-bearing spinel lherzolite PM23-2 with a tabular texture, marked by aligned olivine crystals with scarce widely-spaced subgrain boundaries aligned preferentially normal to the grains' elongation. Phlogopite is undeformed and does not show any preferred orientation. (g–h) Coarse-grained spinel lherzolite PM23-36 with slightly sutured to polygonal olivine–olivine boundaries. Large orthopyroxene crystals bear olivine inclusions and concave limits towards olivine. (i–j) Coarse-grained amphibole-bearing wehrlite PM23-8 with coarse undeformed amphibole crystals exhibiting reaction rims. Clinopyroxene has sutured contacts with olivine. Photomicrograph "i" approximately corresponds to the rotated square in "j". (k–l) Coarse-grained dunite PM23-48 cross cut by amphibole-bearing clinopyroxenite veins with orthopyroxene-rich rims. Ol: olivine, Opx: orthopyroxene, Cpx: clinopyroxene, Amph: amphibole, Phl: phlogopite, Sp: spinel. (For interpretation of the references to color in this figure legend, the reader is referred to the web version of this article.)

Please cite this article as: Zaffarana, C., et al., Microstructures and seismic properties of south Patagonian mantle xenoliths (Gobernador Gregores and Pali Aike), Tectonophysics (2014), http://dx.doi.org/10.1016/j.tecto.2014.02.017

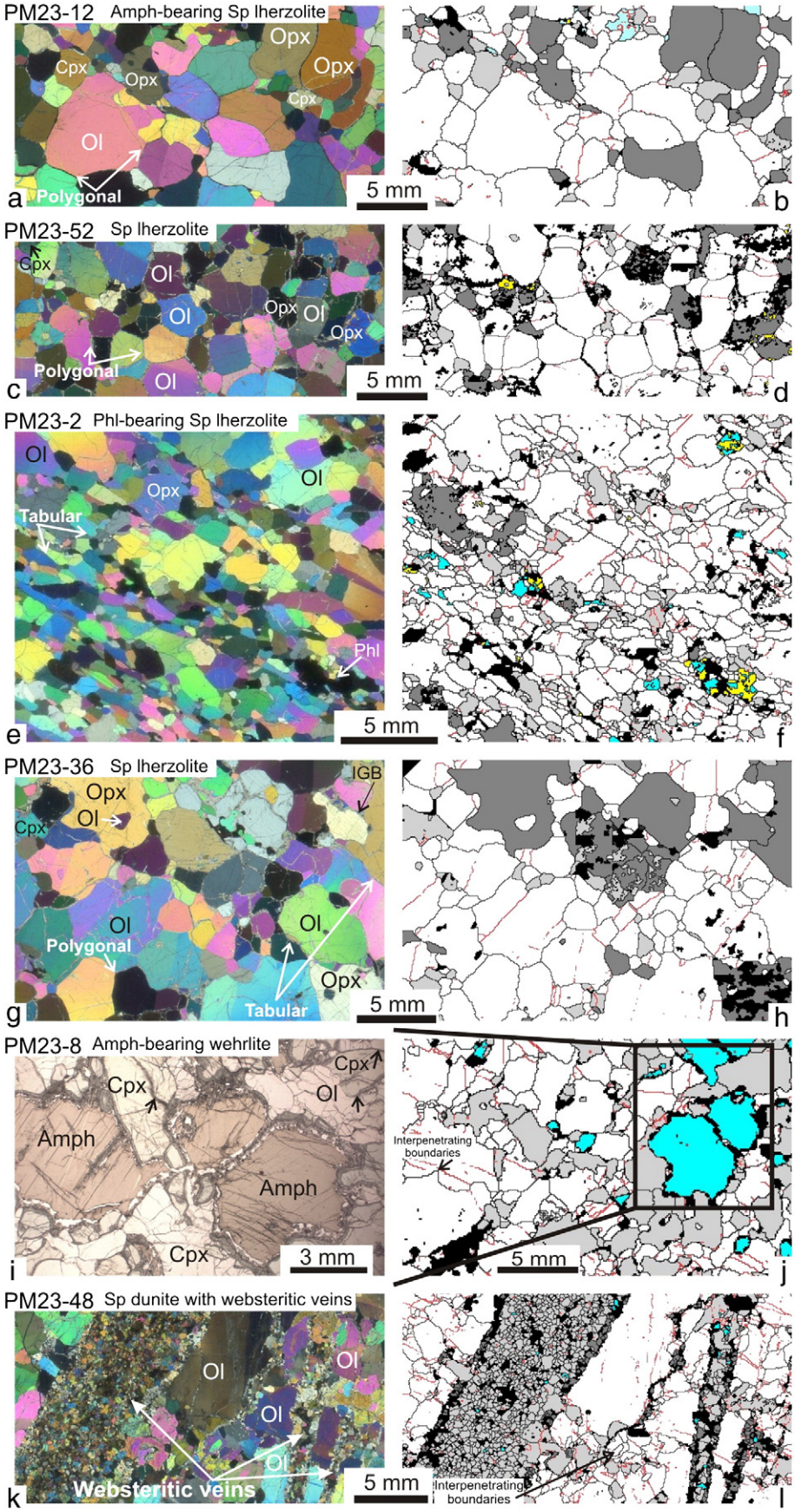

Please cite this article as: Zaffarana, C., et al., Microstructures and seismic properties of south Patagonian mantle xenoliths (Gobernador Gregores and Pali Aike), Tectonophysics (2014), http://dx.doi.org/10.1016/j.tecto.2014.02.017

6.1. Gobernador Gregores

Most Gobernador Gregores peridotites have coarse granular microstructures (Fig. 6a–d, g–h). Wehrlites and dunites tend to show coarser grains (Fig. 6i–l). The phlogopite-bearing spinel lherzolite PM23-2 displays, however, a tabular microstructure, which is particularly well-expressed in finer grained domains, where olivine crystals may have aspect ratios up to 1:6, (Figs. 5b; 6e–f). Finally, spinel lherzolites PM23-21 and PM23-21 have intermediate microstructures, displaying an olivine SPO, but no well-developed crystal faces, or a few subhedral olivine crystals, respectively (Table 2).

In all peridotites, olivine crystals display few widely spaced, but well-developed subgrain boundaries, which in tabular crystals are normal to the elongation (Fig. 6). Olivine grain shapes range from anhedral to subhedral, with straight to gently curved grain boundaries. Interpenetrating olivine–olivine grain boundaries, characteristic of grain boundary migration, are also present. The latter are more common in the wehrlites and in the dunite (Fig. 6i–l). Small rounded pyroxene inclusions in olivine are also common.

Orthopyroxene (enstatite) occurs as irregularly shaped crystals with no shape preferred orientation and grain sizes ranging from 1 to 10 mm. The larger orthopyroxene crystals have concave grain boundaries with embayments filled by olivine and often contain olivine inclusions (Fig. 6g–h). Smaller crystals are often observed along olivine–olivine grain boundaries or triple junctions (Fig. 6a–h). Large orthopyroxenes may show exsolutions and undulose extinction, but these features are not ubiquituous.

Clinopyroxene usually occurs as small interstitial crystals (1–3 mm) in the lherzolites, whereas in the wehrlites clinopyroxene forms large, irregularly shaped crystals (up to 5 mm wide, Fig. 6i–j). It shows no intracrystalline deformation features and has dominantly concave boundaries towards olivine (Fig. 6a–l). In the wehrlites, clinopyroxene may have olivine inclusions (Fig. 6i–j). In the phlogopite-bearing spinel lherzolite (sample PM23-2), clinopyroxene shows spongy rims (arrows in Fig. 6i).

Spinel crystals are interstitial, having irregular, highly cusped shapes. They may have olivine inclusions and display reaction rims. Amphibole (pargasite), when present, forms crystals of ~2–5 mm diameter with convex borders towards the other minerals and with reaction rims (Fig. 6i). It is usually associated with pyroxenes and may show spinel or olivine inclusions. Phlogopite is present only in spinel lherzolite PM23-2 (Fig. 6e–f), occurring as small isolated crystals (1 mm wide). Both amphibole and phlogopite appear undeformed and do not have any preferred orientation.

In the dunite PM23-48 (Fig. 6k–l) clinopyroxenite veins with orthopyroxene-rich reaction walls crosscut the coarse-grained dunite. Small (0.5 mm) amphibole crystals are associated with the clinopyroxene in the veins.

6.2. Pali Aike

Pali Aike peridotites are medium to coarse-grained with granular to tabular microstructures (Figs. 5 and 7, Table 2). Intermediate microstructures, characterized by either a strong tabular tendency (Fig. 5d) or by an olivine shape-preferred orientation (SPO) but not accompanied by well-developed crystallographic faces (Fig. 5c), are more common than in Gobernador Gregores; they represent ~50% of the studied samples (Table 2). In these peridotites, olivine crystals may have aspect ratios up to ~1:5 (Fig. 5b–d). A compositional banding, defined by the alignment of garnet crystals, may parallel the olivine SPO (Fig. 7i–j). No systematic variation of microstructure was observed between the garnet and spinel peridotites and the spinel peridotites.

Olivine crystals, independent of the microstructure, exhibit rare widely spaced, but well-developed subgrain boundaries, which are preferentially oriented normal to grain elongation (Fig. 7a, l). Olivine–olivine grain boundaries tend to be straight or gently curved, often forming 120° triple junctions (Fig. 7c–d).

Orthopyroxene (enstatite) has highly irregular shapes and variable grain sizes, but may attain up to 5 mm in diameter (Fig. 7b,l). It occurs either as isolated crystals (Fig. 7d,j) or forming aggregates. Large orthopyroxene crystals may bear rounded olivine inclusions and show undulose extinction and exsolutions, whereas the smaller crystals are normally devoid of intracrystalline deformation features. Orthopyroxene–olivine grain boundaries are usually concave towards olivine (Fig. 7a–d), with orthopyroxene sometimes forming cusps that fill olivine–olivine grain boundaries (Fig. 7b; e–f). Orthopyroxene rims surrounding another orthopyroxene with a different crystallographic orientation are locally observed (Fig. 7e). The phlogopite-bearing garnet–spinel lherzolite shows a domain strongly enriched in orthopyroxene, where the latter shows convex boundaries towards olivine (Fig. 7g–h).

Clinopyroxene is present as small to medium-size irregularly shaped crystals (1 to 5 mm wide). It mainly occurs as isolated crystals, but ortho- and clinopyroxene aggregates are locally observed (Fig. 7g, h). The larger clinopyroxene crystals show interpenetrating boundaries with olivine (Fig. 7a–b). The smaller crystals usually occur along olivine–olivine grain boundaries (Fig. 7d,k) or at triple junctions (Fig. 7d,l). Clinopyroxene is usually devoid of intracrystalline deformation features, like undulose extinction or kinks. Some crystals contain exsolutions.

Garnet appears as slightly elongated crystals with irregular shapes, occurring either isolated or in aggregates elongated parallel to the foliation defined by olivine shape preferred orientation (Fig. 7l). Garnet crystals typically have spinel in their cores, suggesting cooling and/or decompression (Fig. 7a–h). They also show very fine-grained kelyphitic rims. In the garnet and spinel peridotites, spinel is usually surrounded by garnet, whereas in the spinel peridotites spinel forms small isolated crystals with holy leaf shapes, similar to spinel in Gobernador Gregores xenoliths.

Amphibole (pargasite), when present (15% of the samples of Pali Aike), forms small undeformed crystals (maximum diameter ~3 mm) with convex boundaries towards the other minerals (Fig. 6a–b). Phlogopite partially surrounds orthopyroxene crystals. Neither amphibole nor phlogopite displays a shape preferred orientation or intracrystalline deformation features.

7. Crystallographic preferred orientations

7.1. Olivine

The studied samples from the two localities display olivine CPO with variable intensities and symmetries ranging from [100]-fiber to [010]-fiber with a large proportion of orthorhombic patterns (Figs. 8 and 9, Table 2). *Orthorhombic olivine CPO* is characterized by orthogonal point concentrations of [100], [010] and [001], with stronger concentrations of the [100] and the [010] axes, which result in dominant point (P) distributions for both [100] and [010] axes (Fig. 9a). The [001] axis is generally more dispersed and it falls in the R (random) field for nearly all samples. BA indices for orthorhombic samples range from 0.4 to 0.6 (Fig. 9b). *[100]-fiber olivine CPO* are characterized by a strong point concentration of [100], which shows a point distribution (Fig. 9a). The other two axes form incomplete girdles normal to it; [010] usually has a girdle (G) distribution in the RPG diagram (Fig. 9a). The BA index for these CPO is between 1 and 0.6 (Fig. 9b). *[010]-fiber olivine CPO* are characterized by a point concentration of [010] and girdles of [100] and [001] with weak maxima at 90° to each other. These samples tend to fall in the P (point) field for the [010] axis and in the G (girdle) field for the [100] axis (Fig. 9a). BA indices for [010]-fiber olivine CPO are between 0 and 0.4 (Fig. 9b). Gobernador Gregores peridotites have mainly [100]-fiber and orthorhombic olivine CPO. Only one sample (the phlogopite-bearing spinel lherzolite) has a [010]-fiber olivine CPO (Fig. 9b). In contrast, in Pali Aike peridotites the three different fabric types are almost

Please cite this article as: Zaffarana, C., et al., Microstructures and seismic properties of south Patagonian mantle xenoliths (Gobernador Gregores and Pali Aike), Tectonophysics (2014), http://dx.doi.org/10.1016/j.tecto.2014.02.017

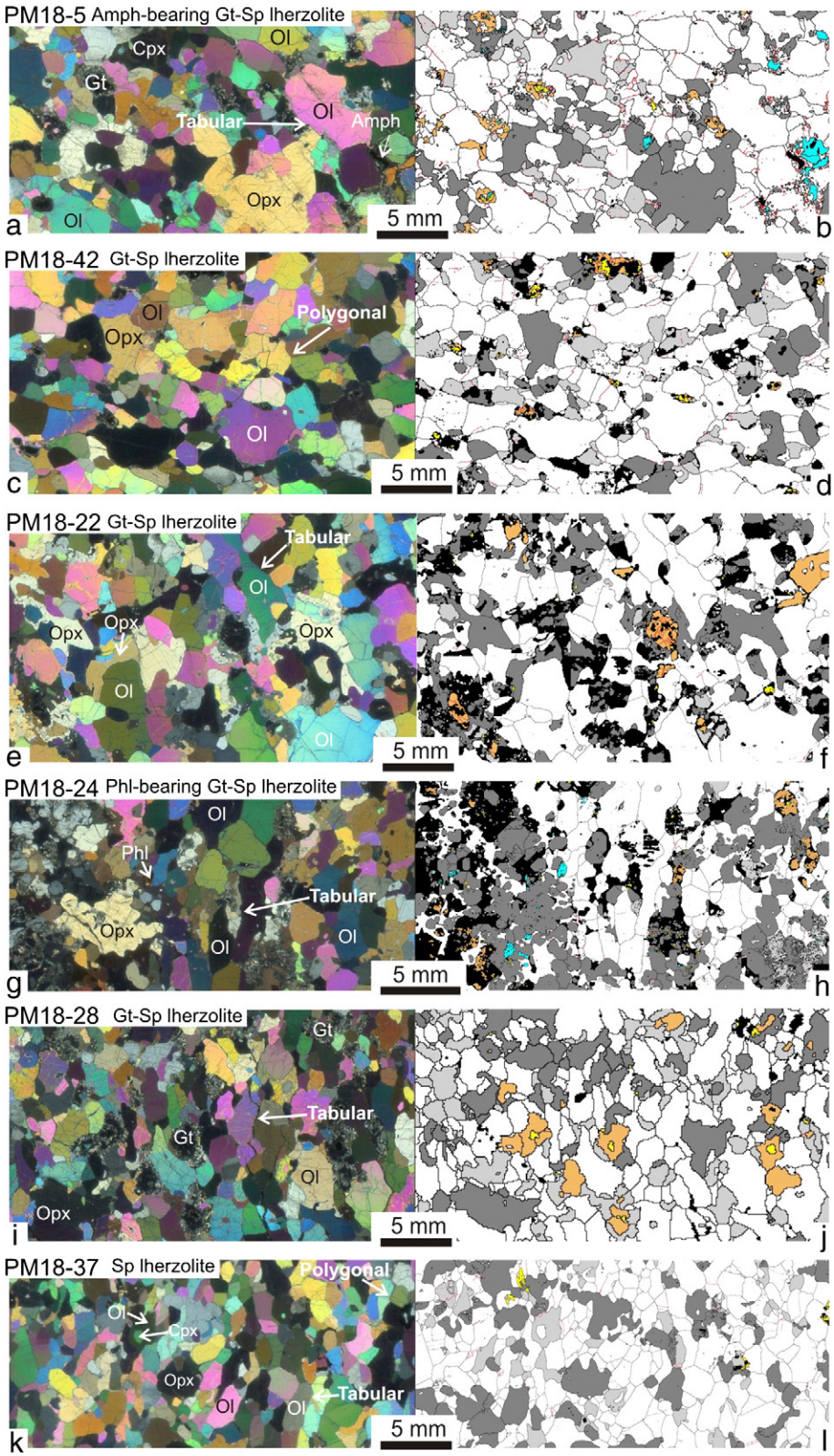

Fig. 7. Typical microstructures of Pali Aike peridotites. Left column: photomicrographs in cross-polarized light, right column: modal composition and grain boundary maps; olivine is shown in white, pyroxenes in gray (orthopyroxene: dark gray, clinopyroxene: light gray), spinel in yellow, garnet in orange, hydrated phases (either amphibole or phlogopite) in light blue, non-indexed points in black. Grain boundaries (misorientations angles > 15°) are shown in black, subgrain boundaries (misorientations between 2 and 15°) are marked in red. (a–b) Amphibole-bearing gt-sp lherzolite PM18-5 showing pyroxenes with irregular shapes, olivines with slightly sutured to polygonal grain boundaries, and rare oriented tabular olivine crystals defining a foliation. (c–d) Coarse-grained gt-sp lherzolite PM18-42 displaying elongated olivine crystals with irregular shapes. (e–f) Garnet spinel lherzolite PM18-22 with an olivine SPO, but no well-developed crystallographic faces, as well as, secondary orthopyroxene enclosing both olivine and preexisting orthopyroxene. (g–h) Phlogopite-bearing gt-sp lherzolite PM18-24 displaying a strong olivine SPO, which is cross-cut by orthopyroxene crystals showing convex boundaries towards olivine. (i–j) Gt-sp lherzolite PM18-28 showing slightly elongated olivine crystals with sutured grain boundaries and pyroxenes with very irregular shapes. (k–l) Sp lherzolite PM18-37 with well developed tabular texture. Ol: olivine, Opx: orthopyroxene, Cpx: clinopyroxene, Amph: amphibole, Phl: phlogopite, Sp: spinel, Gt: garnet. (For interpretation of the references to color in this figure legend, the reader is referred to the web version of this article.)

Please cite this article as: Zaffarana, C., et al., Microstructures and seismic properties of south Patagonian mantle xenoliths (Gobernador Gregores and Pali Aike), Tectonophysics (2014), http://dx.doi.org/10.1016/j.tecto.2014.02.017

equally represented: 8 samples have [010]-fiber olivine CPO, 7 samples have [100]-fiber olivine CPO, and 5 show orthorhombic olivine CPO (Table 2 and Fig. 8c–d).

Olivine CPO in Gobernador Gregores peridotites are in average stronger than in Pali Aike peridotites, with the highest J-index values (J > 6) displayed by the anhydrous spinel lherzolites (Fig. 9c–d).

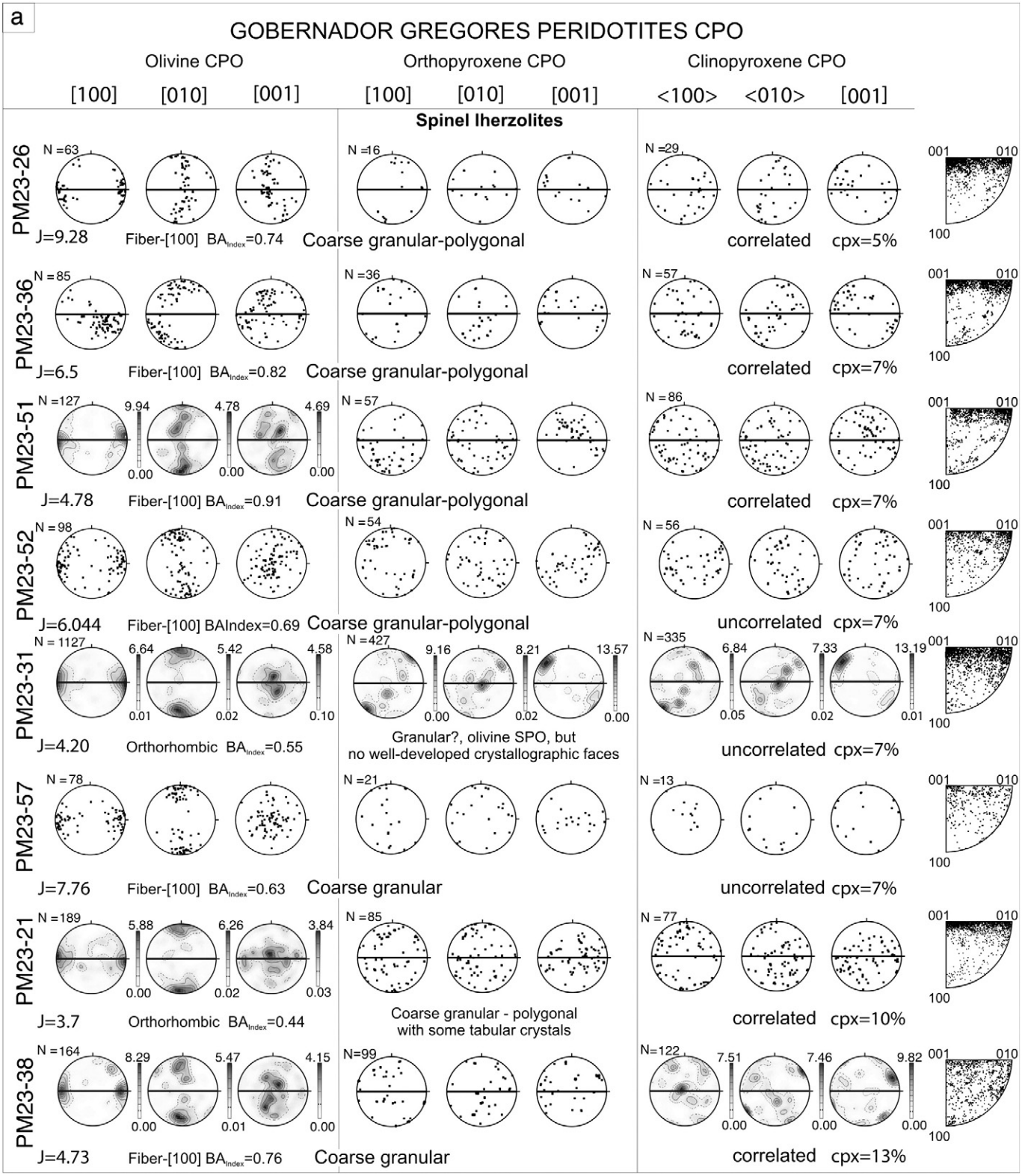

Fig. 8. Crystallographic preferred orientation (CPO) of olivine, orthopyroxene and clinopyroxene in the peridotites of Gobernador Gregores (a, b) and Pali Aike (c, d). Pole figures are ordered as a function of increasing clinopyroxene modal content. Lower hemisphere equal area stereographic projections, contours at multiples of uniform distribution. Pole figures with less than 100 measurements were not contoured. For easy comparison, all CPO data were rotated in a standard position, with the maximum concentrations of olivine [100] and [010] axes parallel to the horizontal E–W and N–S directions, respectively. Olivine CPO classification and the relation between olivine and pyroxenes CPO (correlated/not correlated) are signaled for each sample. Main textural characteristics of each sample are also indicated. Rightmost column shows an inverse pole figure displaying the rotation axes that accommodate low-angle misorientations (<15°).

Please cite this article as: Zaffarana, C., et al., Microstructures and seismic properties of south Patagonian mantle xenoliths (Gobernador Gregores and Pali Aike), Tectonophysics (2014), http://dx.doi.org/10.1016/j.tecto.2014.02.017

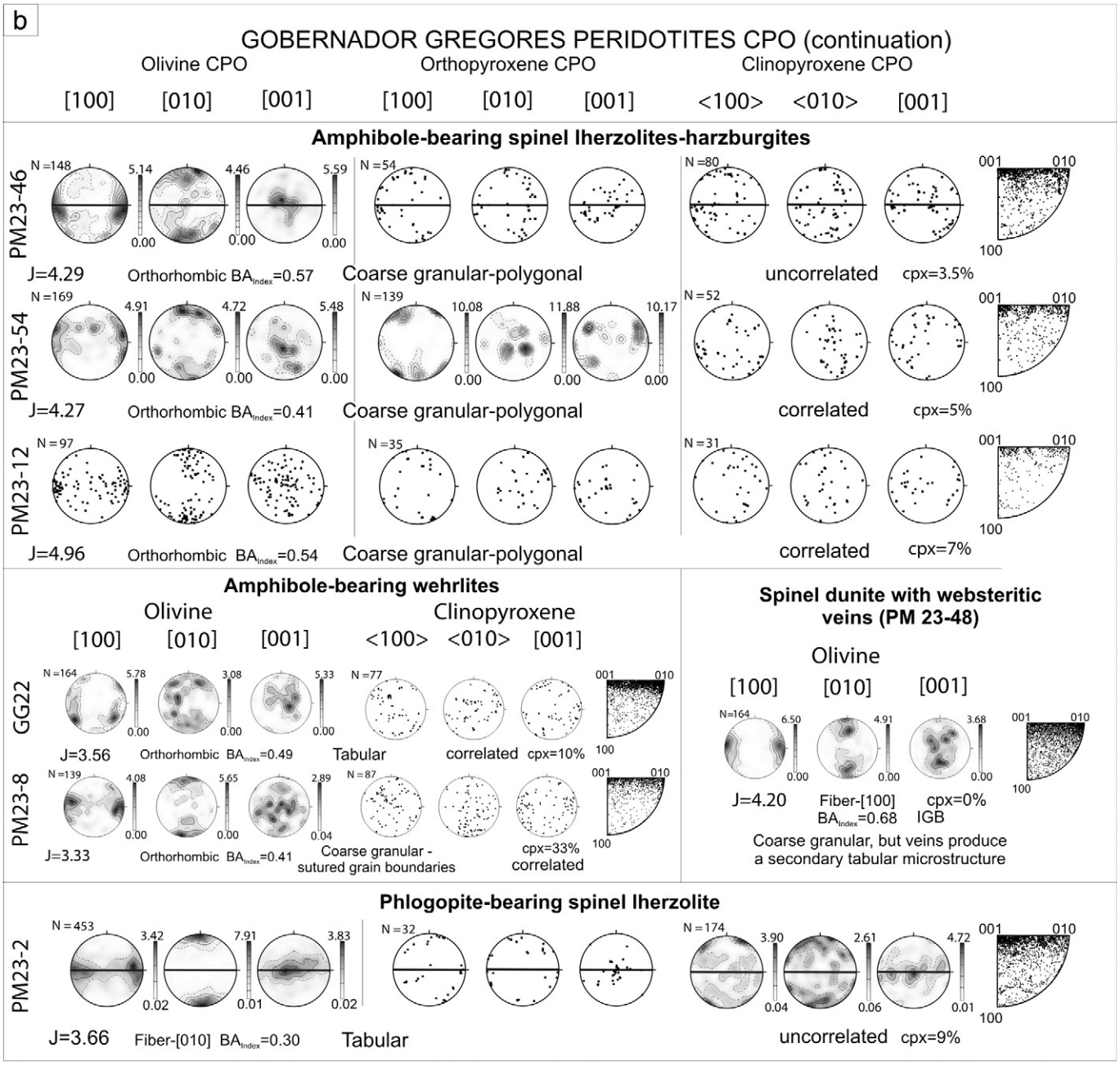

Fig. 8 (*continued*).

Gobernador Gregores amphibole-bearing spinel peridotites generally have lower fabric strength than their anhydrous counterparts (Fig. 9b), but this relation may be biased by the limited number of hydrated samples studied. In general, peridotites with olivine contents <65% or clinopyroxene contents >15% tend to have weak olivine CPO (J indices < 4, Fig. 9c–d). There is no correlation between the orthopyroxene content and the olivine CPO strength.

There is no clear correlation between modal composition and the olivine CPO symmetry, but [100]-fiber and orthorhombic olivine CPO predominate for olivine contents >70% (Fig. 10 and Table 2). Samples with fiber-[010] olivine CPO (BA index < 0.4) have tabular or granular microstructures with a tabular tendency (Table 2). In these peridotites, the [010] concentration is roughly perpendicular to the foliation defined by olivine elongation (Fig. 8c–d).

7.2. Orthopyroxene and clinopyroxene CPO

Analysis of the pyroxenes CPO was hindered in some samples by the small number of grains present in the thin section, which may have resulted in overestimation of the CPO strength. However, where enough grains for a statistic analysis could be measured, orthopyroxene and clinopyroxene CPO are systematically weaker than olivine CPO (Fig. 8). Ortho- and clinopyroxene CPO are usually coaxial with the [001] axes usually showing the strongest concentration, but clinopyroxene orientations tend to be more dispersed (Fig. 8). Comparison of the pyroxene and olivine CPO allows discriminating between samples where the [100] olivine axis maximum is parallel to the [001] pyroxene axis ("correlated" samples, Fig. 8, Table 2) and samples where the maximum concentration of pyroxene [001] axes either

Please cite this article as: Zaffarana, C., et al., Microstructures and seismic properties of south Patagonian mantle xenoliths (Gobernador Gregores and Pali Aike), Tectonophysics (2014), http://dx.doi.org/10.1016/j.tecto.2014.02.017

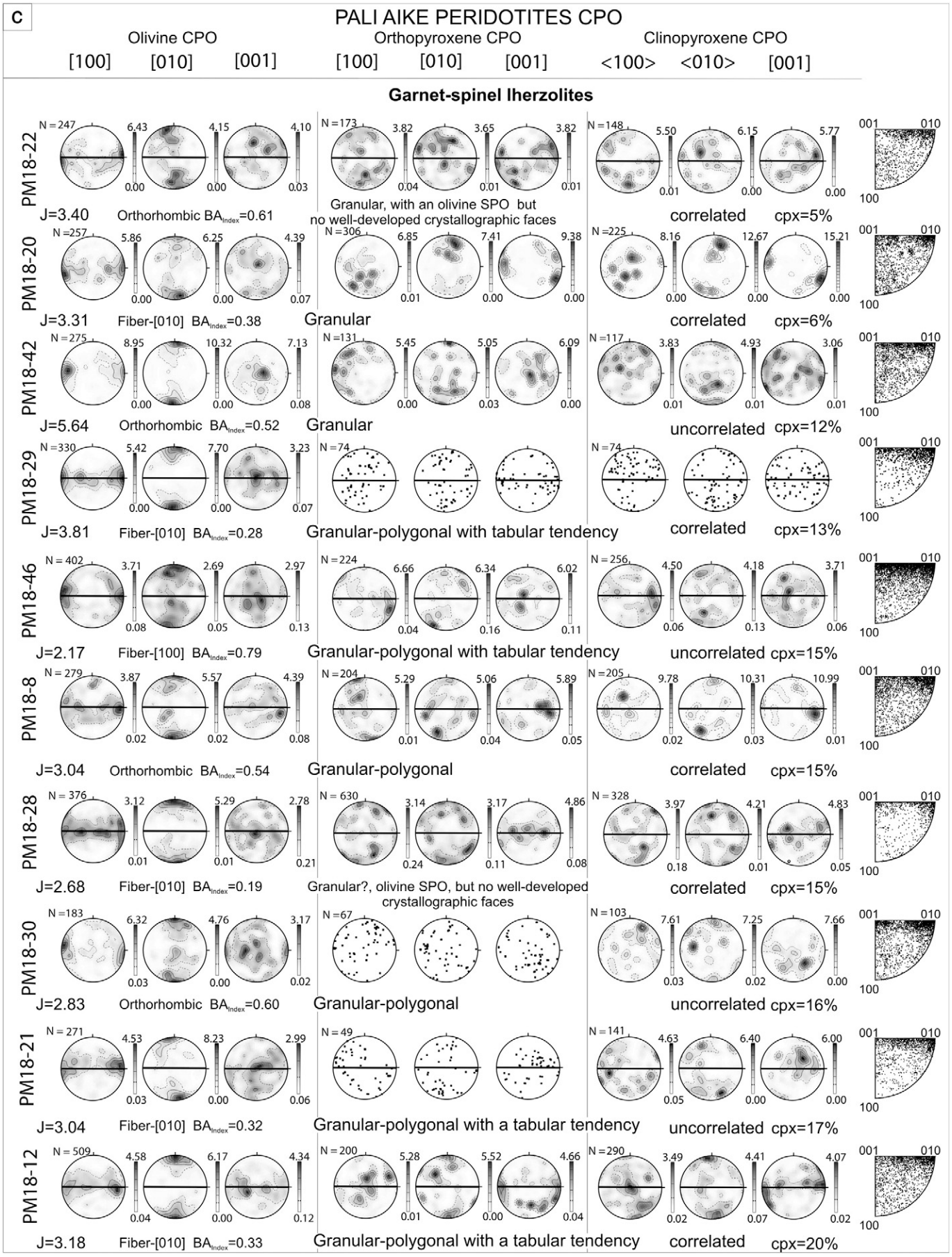

Fig. 8 (*continued*).

Please cite this article as: Zaffarana, C., et al., Microstructures and seismic properties of south Patagonian mantle xenoliths (Gobernador Gregores and Pali Aike), Tectonophysics (2014), http://dx.doi.org/10.1016/j.tecto.2014.02.017

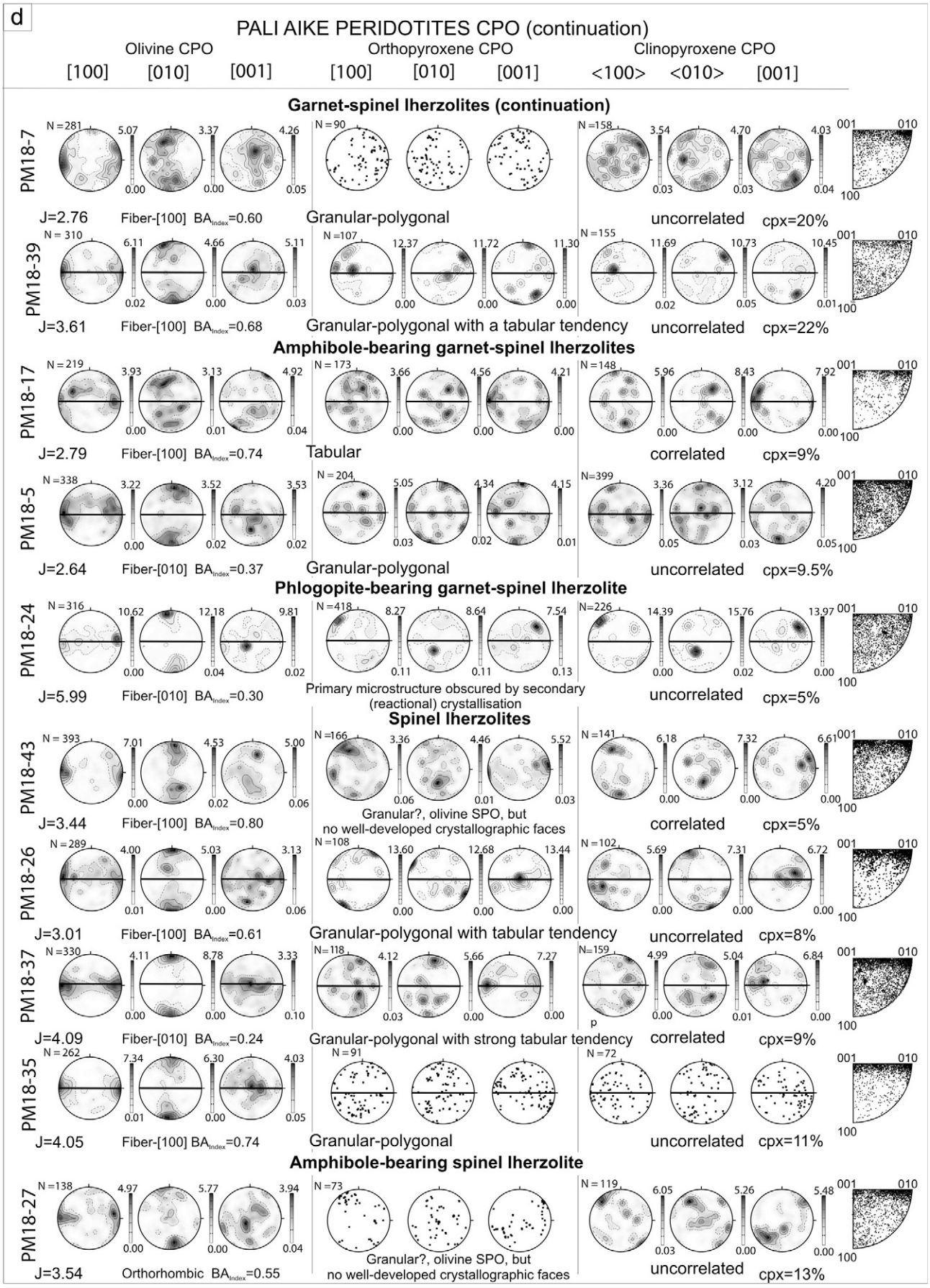

Fig. 8 (*continued*).

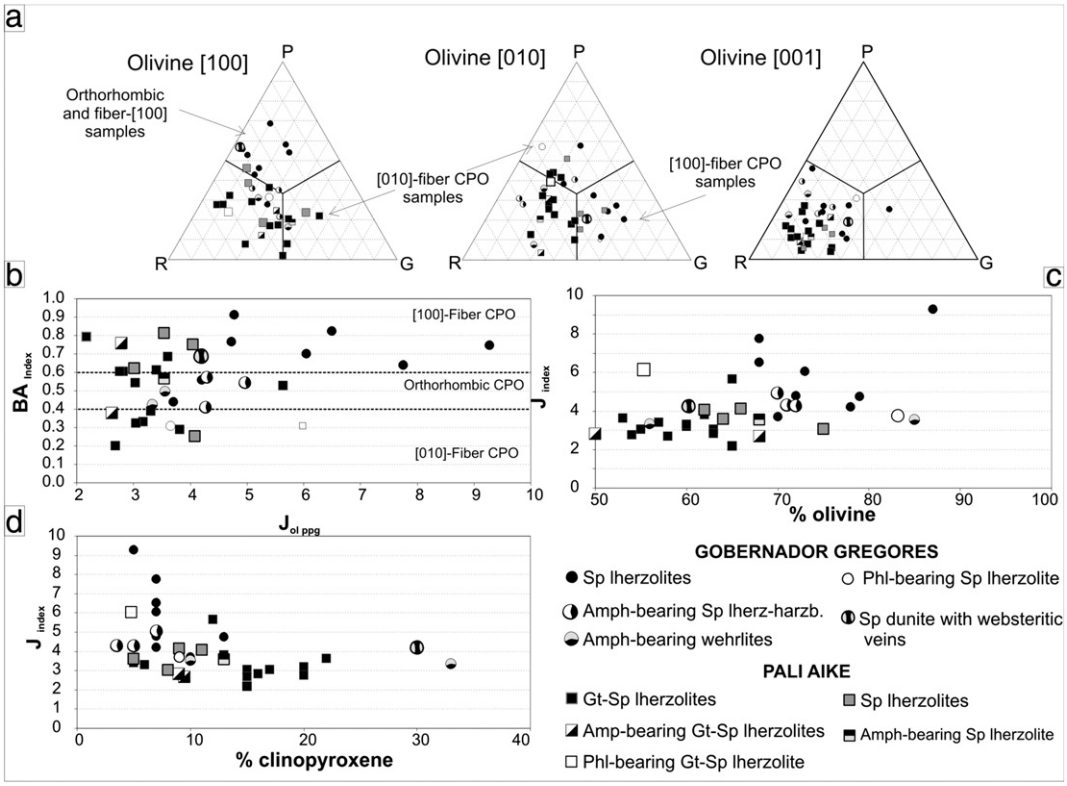

Fig. 9. Olivine CPO strength and symmetry. (a) Olivine CPO symmetry expressed as the proportion of point (P), girdle (G) and random (R) components for [100], [010] and [001] crystallographic axes. (b) Relation between the olivine CPO symmetry (BA indices) and strength (J indices calculated using one orientation datum per grain). Olivine CPO strength (J indices) function of the proportion (vol.%) of (c) olivine and (d) clinopyroxene in each sample.

coincides with the [001] olivine axis maximum or is very weak ("uncorrelated" samples, Fig. 8, Table 2). 64% of the Gobernador Gregores and 50% of the Pali Aike samples have correlated olivine and pyroxene CPO (Fig. 8, Table 2). In these samples, the maximum concentration of [100] of orthopyroxene and of [010] of clinopyroxene, though weak, tends to align with the [010] maximum of olivine. There is no clear relation between the alignment of the olivine and pyroxene CPOs and the strength or symmetry of the olivine CPO (Fig. 10).

Finally, the websteritic veins that crosscut the dunite from Gobernador Gregores (sample PM23-48, Table 2, Fig. 11) exhibit a clear clinopyroxene CPO with [001] axes parallel to the strike of the veins. The dunite has a [100]-fiber olivine CPO with the [100] maximum parallel to the strike of the websteritic veins.

7.3. Amphibole and phlogopite CPO

Amphibole and phlogopite CPO are very weak. However, due to their low modal contents, the number of measured grains is too low to be statistically meaningful, so they are not shown. However, both amphibole and phlogopite [001] axes tend to parallel the pyroxenes [001] axis, suggesting topotaxial relations for these reactional products.

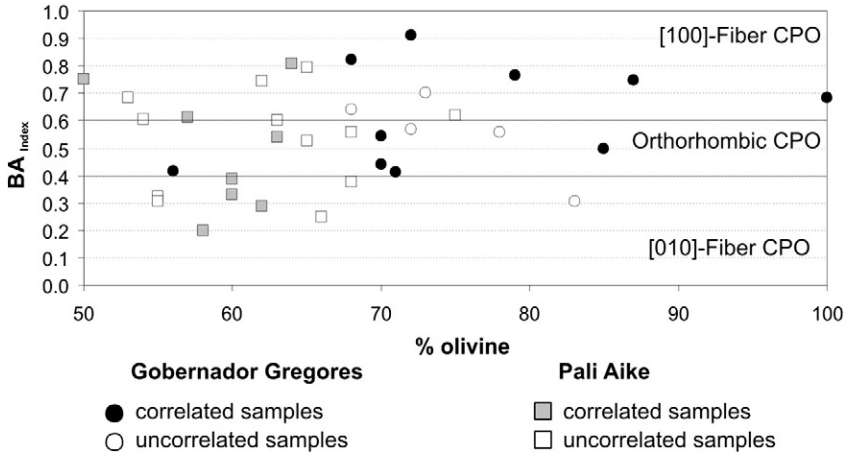

Fig. 10. Olivine CPO symmetry (indicated by the BA indices) as a function of the modal proportion of olivine (vol.%). Filled symbols indicate samples that have correlated olivine and orthopyroxene CPO and open symbols samples in which the CPO of the two minerals are uncorrelated.

Please cite this article as: Zaffarana, C., et al., Microstructures and seismic properties of south Patagonian mantle xenoliths (Gobernador Gregores and Pali Aike), Tectonophysics (2014), http://dx.doi.org/10.1016/j.tecto.2014.02.017

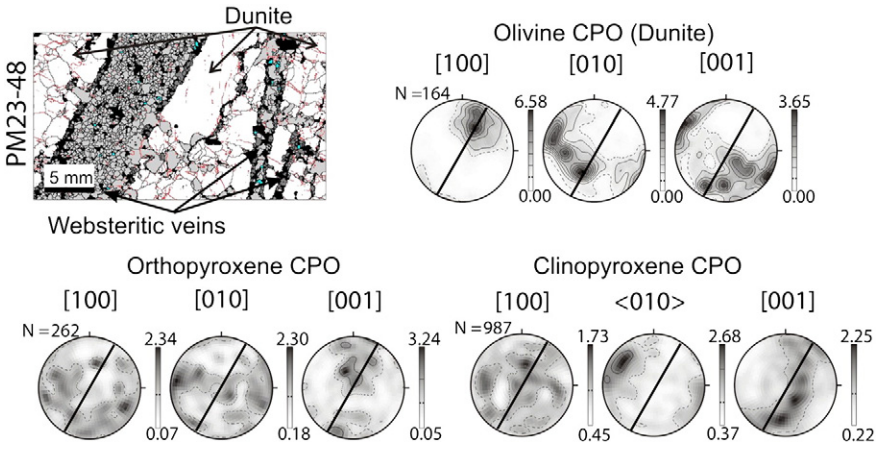

Fig. 11. Textural data for the dunite crosscut by websteritic veins of Gobernador Gregores (sample PM23-48): modal composition and grain boundary map (color legend as in Figs. 3 and 4) and pole figures showing the olivine, orthopyroxene and clinopyroxene CPO in the thin section reference frame. Full line on the pole figures indicates the strike of the websteritic veins. Lower hemisphere equal area stereographic projections, contours at one multiple of a uniform distribution.

8. Seismic properties

Seismic properties of Gobernador Gregores and Pali Aike peridotites were calculated at ambient P, T conditions for both individual samples and for "average" samples for each locality obtained by adding up the individual samples CPO data in a common reference frame (the one used for displaying the CPO in Fig. 8). Results for the individual samples, which are very homogeneous, are summarized in Table 2. The average samples' properties (Fig. 12a–b, Table 2) correspond to the maximum anisotropy that can be expected at each locality, since this calculation assumes a coherent deformation (same kinematics) for all samples.

The average samples for the two localities, independently of their composition, show similar patterns of variation of seismic velocities and anisotropies relative to the olivine CPO, which are typical of mantle peridotites (Fig. 12a–b). In the analyzed samples, P-waves as well as the slowest shear waves (S_2) are fastest when propagating parallel to the maximum concentration of olivine [100] axes and slowest when traveling parallel to the maximum concentration of [010] axes (which is perpendicular to the foliation in the tabular peridotites). Significant P and S_2 propagation anisotropies are observed in any plane containing the [100] maximum. Low anisotropies are, in contrast, sampled by P and S_2 waves propagating normal to this maximum, that is, to the flow direction. Maximum propagation anisotropies are generally lower for the fast shear waves (S_1) than for the slow (S_2) shear waves, and Vs_1 patterns more complex than Vs_2 patterns (Fig. 12a–b). The fast shear wave S_1 is always polarized parallel to the olivine [100] maximum and the maximum birefringence is observed for shear waves propagating at high angle to both the [100] and [010] maxima (Fig. 12a–b).

The stronger olivine CPO of Gobernador Gregores peridotites results in higher maximum P- and S-wave anisotropies relatively to Pali Aike peridotites (Fig. 13a–b). Maximum seismic anisotropies (AVs, AVp, AVs_1, AVs_2) also increase with olivine content and, in Gobernador Gregores peridotites, decrease with increasing clinopyroxene content (Fig. 13c–f). The latter relation is coherent with the decrease in olivine CPO strength for high clinopyroxene contents (>15%, Fig. 9d). Amphibole-bearing spinel peridotites of Gobernador Gregores and the phlogopite-bearing lherzolite of Pali Aike tend to show slightly lower seismic anisotropies than their anhydrous counterparts (Fig. 13, Table 2). The highest anisotropies are thus observed for the spinel lherzolites from Gobernador Gregores (P-wave anisotropy of 11.9%, S-wave polarization anisotropy of 7.4%, Table 2).

The change in olivine CPO symmetry does not alter the magnitude of the seismic anisotropy (AVs, AVp, AVs_1, AVs_2; Fig. 13g–h). The spinel peridotites of Gobernador Gregores show stronger seismic anisotropies associated with orthorhombic to [100]-fiber olivine CPO (Fig. 13g–h). However these samples also show strong olivine CPO (Fig. 9b), which explains their high seismic anisotropy. Change in olivine CPO symmetry from [100]-fiber or orthorhombic to [010]-fiber changes slightly the seismic anisotropy patterns. In particular, while in peridotites with a [100]-fiber or an orthorhombic olivine CPO the apparent isotropy direction for S-wave (AVSmin orientation) is at low angle to the [100] maximum (Fig. 14a), in peridotites with a [010]-fiber olivine CPO it is at low angle to the [010] maximum (Fig. 14b). However, [010]-fiber seismic anisotropy patterns would only be detected by seismological surveys if this type of olivine CPO predominates in the upper mantle, since the average samples seismic properties display an orthorhombic symmetry with an apparent isotropy direction for S-waves at low angle to the [100] maximum (Fig. 12).

9. Discussion

9.1. Relations between deformation, annealing, and reactive melt percolation in the South Patagonian mantle lithosphere

The coarse-grained microstructures, the low density of intracrystalline deformation features in olivine and pyroxenes, and the polygonal grain shapes, characterized by straight grain boundaries forming 120° triple junctions indicate that all studied peridotites were affected by extensive annealing (static recrystallization and grain growth). This extensive annealing implies effective diffusion due to either high temperatures (consistent with some but not all equilibrium thermobarometry data) or slow cooling in stable subcontinental mantle lithosphere. Strongly annealed microstructures predominate, for instance, in cratonic xenolith suites (e.g., Baptiste et al., 2012; Vauchez et al., 2005).

The well-developed olivine and, in most samples, pyroxenes CPO suggests, however, that annealing was preceded by deformation through dislocation creep. As observed in previous studies (e.g., Baptiste et al., 2012; Tommasi et al., 2008; Vauchez et al., 2005), static recrystallization did not erase the preexisting CPO. Dominant activation of [100] glide is supported by the axial symmetry of the [100]-fiber CPO and by the stronger concentration of [100] than [001] in the orthorhombic and [010]-fiber CPO samples (Fig. 8). Dominant activation of the [100]{0kl} slip systems in olivine can also be inferred from the preserved (100) olivine subgrain boundaries and from the predominance of <0VW> rotation axes with two maxima parallel to [001] and to [010] accommodating low angle (<15°) misorientations (Fig. 8).

In the correlated peridotites, parallelism between the dominant glide directions of olivine and pyroxenes, i.e., the alignment of the olivine [100] maximum with the pyroxenes [001] maximum, suggests that they were deformed simultaneously. Although weak, the pyroxene CPO in these correlated samples is consistent with deformation by dislocation creep, with dominant activation of [001](100) in orthopyroxene

Please cite this article as: Zaffarana, C., et al., Microstructures and seismic properties of south Patagonian mantle xenoliths (Gobernador Gregores and Pali Aike), Tectonophysics (2014), http://dx.doi.org/10.1016/j.tecto.2014.02.017

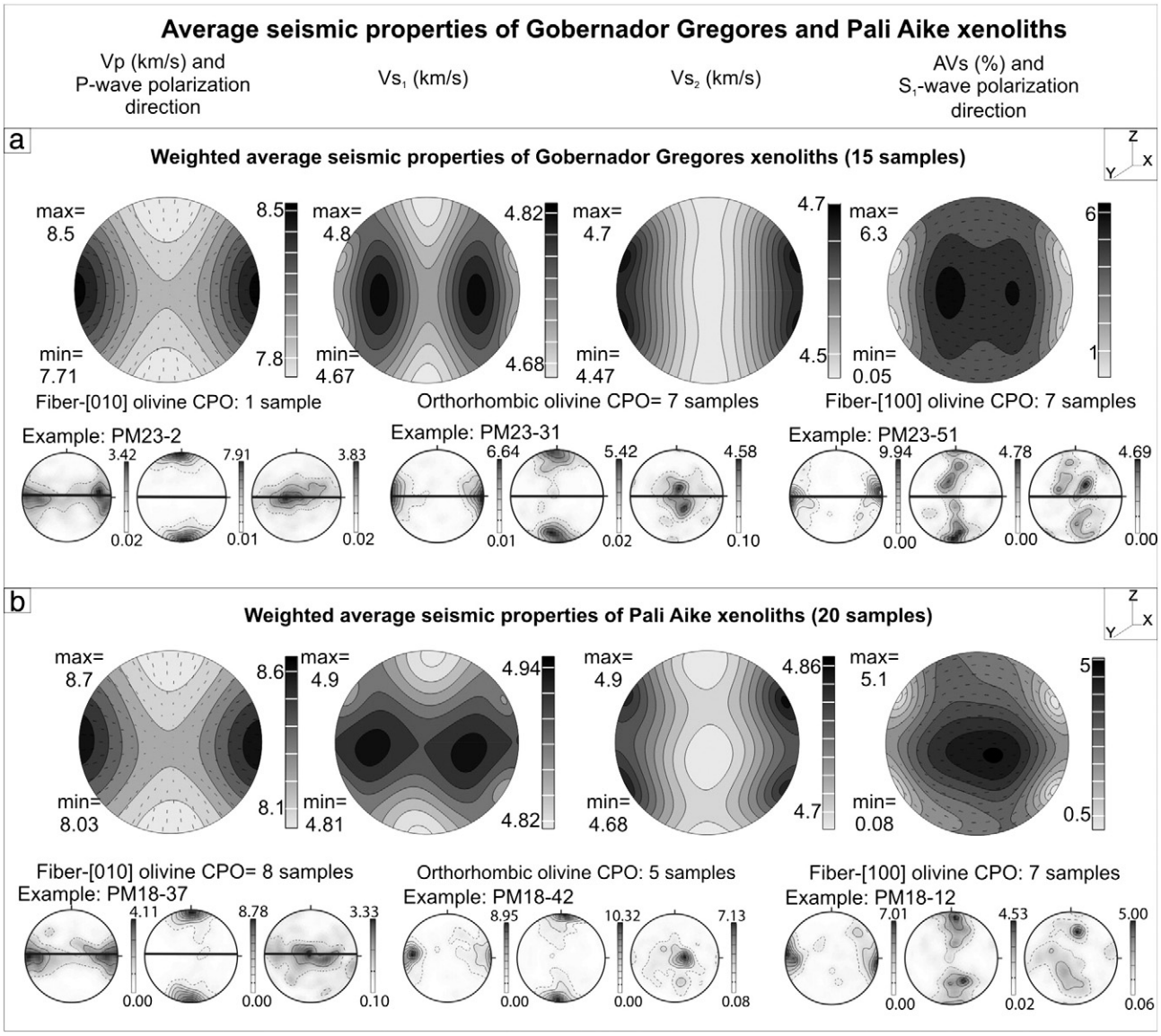

Fig. 12. Calculated seismic properties of "average" samples for Gobernador Gregores (a) and for Pali Aike (b). Average samples were created by adding up the CPO data of the individual samples. Column 1 displays the velocity distribution of the P waves (km/s) together with the P wave polarization direction, columns 2 and 3 display the fast and the slow S wave velocities (Vs_1 and Vs_2, respectively), and column 4 displays S wave polarization anisotropy in percent together with the S_1 wave polarization direction. One example of each olivine CPO type from each locality is added to illustrate the relation between olivine CPO and the anisotropy of seismic properties.

and [001]{110} in clinopyroxene (e.g., Bascou et al., 2002; Frets et al., 2012; Green and Radcliffe, 1972; Van Roermund and Boland, 1981). Limited obliquity (<20°) between the olivine and the pyroxene CPO may result from lower finite strains in the stronger pyroxene crystals.

In contrast, the uncorrelated olivine and pyroxenes CPO (or almost random pyroxenes CPO) observed in 33% of Gobernador Gregores samples and in 50% of Pali Aike samples (Fig. 8 and Table 2), suggests pyroxene addition by post-kinematic reactive melt percolation (e.g., Soustelle et al., 2010). Indeed, although subparallel [001] maximum concentrations for olivine and pyroxene might be produced by common deformation if olivine deforms by dominant [001] glide, dominant activation of [001] glide in olivine is not consistent with the stronger [100] preferred orientation of olivine relative to [001], nor with the misorientation data for low angle boundaries in olivine (cf. discussion above).

Metasomatism by alkaline or carbonatitic magmas in Gobernador Gregores and by subalkaline to tholeitic magmas in Pali Aike had been suggested based on geochemical information (Bjerg et al., 2005; Dantas, 2007; Gorring and Kay, 2000; Laurora et al., 2001; Rivalenti et al., 2004a,b; Stern et al., 1986, 1989). The analysis of clinopyroxene REE patterns of some of the samples of both suites that are studied here (Fig. 2, Dantas, 2007) shows that strong LREE enrichment is associated with the presence of hydrous minerals (amphibole or phlogopite). The lack of intracrystalline deformation features and the random orientation of amphiboles and phlogopite (Figs. 5a, e, i and 6a, e) in the studied samples indicate that their crystallization is post-kinematic, suggesting that geochemical data record mainly the latest metasomatic episodes.

On the other hand, (i) the analysis of the modal compositions, which mostly do not coincide with partial melting trends (Fig. 4) and (ii) the interpenetrating olivine–pyroxene boundaries and the olivine inclusions in pyroxenes (Figs. 6 and 7) displayed by most peridotites from both Gobernador Gregores and Pali Aike clearly imply reactive melt (or fluids) percolation leading to both pyroxene crystallization at the expense of olivine and olivine crystallization at the expense of pyroxenes, function of the composition of the percolating melt/fluid (Kelemen et al., 1997; Le Roux et al., 2007; Morgan and Liang, 2005).

Petrographic features indicating pyroxene crystallization at the expense of olivine are, however, not restricted to samples that show

Please cite this article as: Zaffarana, C., et al., Microstructures and seismic properties of south Patagonian mantle xenoliths (Gobernador Gregores and Pali Aike), Tectonophysics (2014), http://dx.doi.org/10.1016/j.tecto.2014.02.017

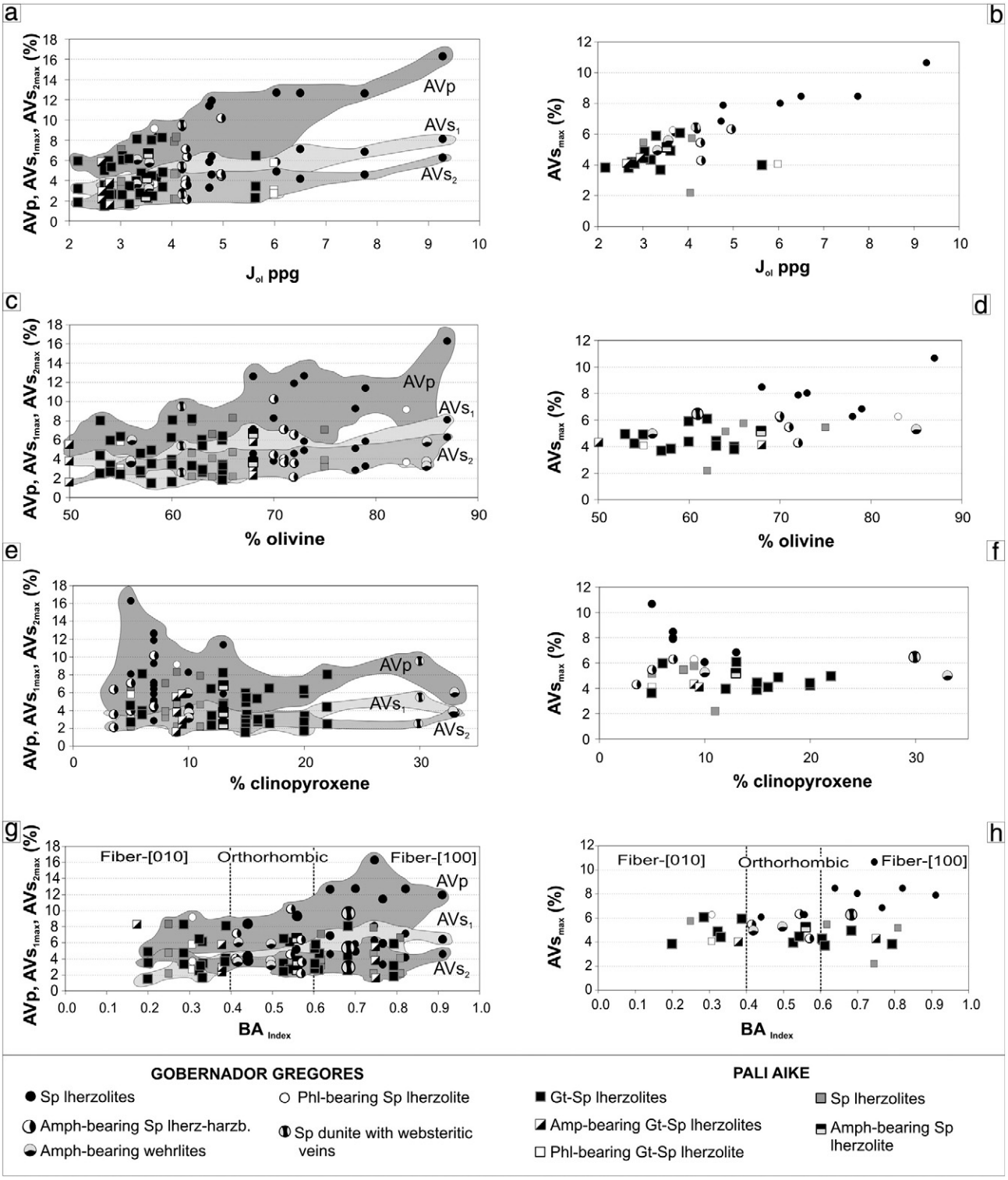

Fig. 13. Seismic anisotropies (AVp, AVs_{1max}, AVs_{2max}, AVs_{max}) vs. olivine fabric strength (J_{ol}), olivine and clinopyroxene content and BA_{index}.

uncorrelated olivine and pyroxene CPOs. Two interpretations may thus be proposed: (i) multiple reactive melt percolation episodes with different timings relative to the deformation are recorded within the studied xenoliths or (ii) post-kinematic melt percolation, which, resulted in both overgrowth of preexisting, already oriented pyroxenes (the correlated samples) and in crystallization of new crystals with random orientation (the non-correlated samples). Post-kinematic crystallization of orthopyroxene is, for instance, clearly evidenced by the microstructure of the phlogopite-bearing spinel lherzolite PM18-24 (Fig. 7e–f), which shows correlated olivine and orthopyroxene CPO (Fig. 8d). However, the microstructural relations are not as clear in all studied peridotites and the hypothesis (i) cannot be discarded.

In Gobernador Gregores, the presence of dunites, wehrlites, and websterites clearly indicates multiple episodes of reactive melt percolation leading to either pyroxenes or olivine consumption depending on the melt composition (see references above). The clear olivine CPO of the dunite (Fig. 11) suggests that dunitization was produced by the pre- or synkinematic reactive melt percolation, whereas the sharp

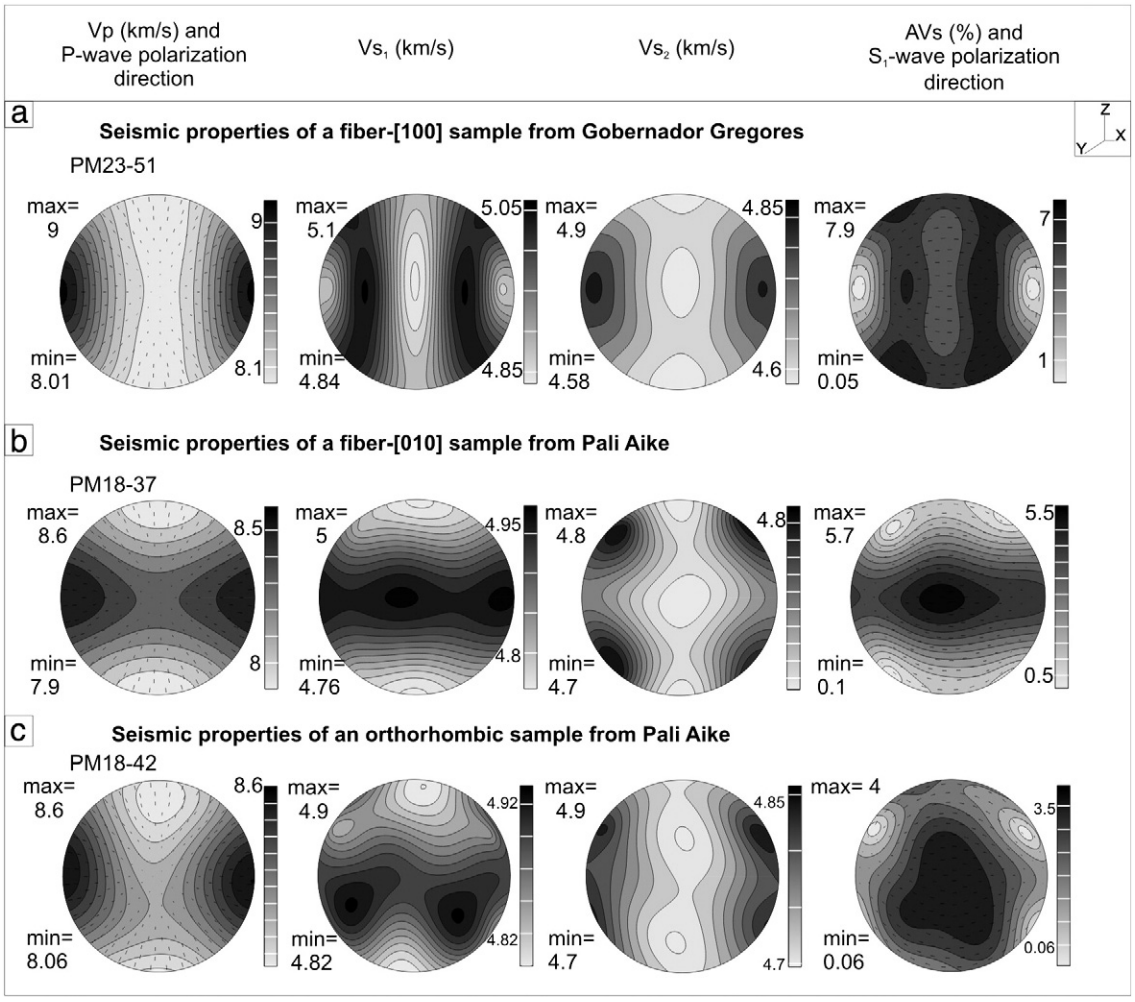

Fig. 14. Seismic properties as a function of the olivine CPO symmetry: (a) sample PM 23-from Gobernador Gregores that has a strong [100]-fiber olivine CPO, (b), sample PM18-37 from Pali Aike that bears a [010]-fiber olivine CPO, and (c) sample PM18-42 Pali Aike that has an orthorhombic olivine CPO.

boundaries of the websterite veins suggest that they formed during a late stage after significant cooling. The preferred alignment of the clinopyroxene [001] and [010] axes parallel and normal to the veins walls, respectively, suggests oriented crystallization controlled by the vein opening or the melt flow. Except for this example, where the websterite formation is clearly a late episode, the relative timing between annealing and reactive melt or fluids percolation cannot be unraveled from the present data.

9.2. Olivine CPO symmetry

Orthorhombic and [100]-fiber CPO patterns predominate in Gobernador Gregores xenoliths (Table 2, Fig. 8). These CPO patterns are also the most common in naturally deformed peridotites (Ben Ismaïl and Mainprice, 1998; Tommasi et al., 2000), as well as in dunites experimentally sheared at high temperature, low pressure and dry conditions (Bystricky et al., 2000; Zhang and Karato, 1995). They result from dominant activation of the [100]{0kl} slip systems under deformation regimes characterized by a well-defined extension direction: simple shear, extrusion, 2D-transpression or transtension (Tommasi et al., 1999).

Pali Aike, in contrast, displays a large proportion of [010]-fiber olivine CPO (Table 2, Fig. 8). Pure [010]-fiber CPO forms in axial shortening (Nicolas et al., 1973) and CPO patterns with a strong [010]-fiber component are characteristic of three-dimensional transpression, even when the simple shear component dominates (Tommasi et al., 1999). However, transpressional deformation should also result in dispersion of orthopyroxene [001] axes in the foliation plane, which is not observed in most studied samples (with the exception of samples PM18-28 and PM18-29, Fig. 8c). Simultaneous activation of [100] and [001] slip systems under high stress, high pressure (>3.5 GPa) or hydrated conditions is another mechanism leading to the formation of [010]-fiber CPO (Jung et al., 2006; Mainprice et al., 2005; Tommasi et al., 2000). However, equilibration pressures are low and significant activation of [001] glide is not supported by misorientation data (Fig. 8).

The common association of [010]-fiber olivine CPO and a tabular tendency in the microstructures (Figs. 4 and 8, Table 2) suggests that anisotropic grain boundary properties may have controlled grain growth during annealing, resulting in strongly anisometric grain shapes and in increasing volume fraction of crystals with [010] normal to the trace of the foliation plane. In kimberlite-born peridotites, static grain growth in the presence of fluids has been proposed as a mechanism leading to the formation of tabular olivine crystals with similar crystallographic features as the ones that produce the tabular textures in the Patagonian xenoliths (Arndt et al., 2010; Drury and Van Roermund, 1989). A similar metasomatism-related process might account for the formation of the tabular textures in the xenoliths from Gobernador Gregores and Pali Aike. However, though many tabular peridotites show high clinopyroxene contents or hydrous phases, not all clinopyroxene-rich or hydrous peridotites have tabular textures

Please cite this article as: Zaffarana, C., et al., Microstructures and seismic properties of south Patagonian mantle xenoliths (Gobernador Gregores and Pali Aike), Tectonophysics (2014), http://dx.doi.org/10.1016/j.tecto.2014.02.017

(Table 2). There is also no relation between the olivine composition and the crystal shapes.

Interestingly, all [010]-fiber samples from Pali Aike show predominance of low angle rotation axes close to [010] (Fig. 8c–d). This points to a higher density of [100](001) edge dislocations in the subgrains that are mainly (100) tilt walls. However, the [010]-fiber CPO implies that the dominant slip plane is (010) instead of (001). This contradiction between dominant slip planes inferred from the CPO and from the analysis of low-angle misorientations has also been reported in previous microstructural studies on peridotites (Falus et al., 2008; Soustelle et al., 2010; Tommasi et al., 2008); it implies that dislocations preserved in subgrain boundaries may not be representative of the most active slip systems, and that the inference of slip systems activity should not be based solely on misorientation data.

9.3. Seismic properties of the South Patagonian mantle lithosphere

Both localities show rather homogeneous seismic properties, which are typical of mantle rocks deformed under high temperature and low to intermediate pressure conditions by dislocation creep with dominant activation of [100] glide. The maximum intensity of seismic anisotropy for both S-waves polarization and P- and S-waves azimuthal anisotropy depends essentially on the strength and symmetry of the olivine CPO and on the olivine content, as observed in previous studies (e.g., Ben Ismaïl and Mainprice, 1998). Unless it results in significant changes in the modal composition (strong enrichment in clinopyroxene or hydrous phases), reactive melt or fluids percolation under static conditions has therefore only a minor effect on the seismic anisotropy (Figs. 12–13), slightly reducing the anisotropy due to the relative decrease in olivine content.

If, as proposed in the previous section, reactive melt or fluid percolation results in a change in the olivine CPO symmetry towards [010]-fiber patterns, it might also change the seismic anisotropy signature as the latter shows an apparent isotropy for S-waves propagating normal to the foliation, instead of subparallel to the lineation (Fig. 14, Vauchez et al., 2005; Bascou et al., 2008). However, comparison of the average seismic properties for Gobernador Gregores, where orthorhombic and [100]-fiber predominate, and for Pali Aike, where all three fabric symmetries contribute more or less equally to the average sample (Fig. 12), shows that the [010]-fiber patterns have to dominate to produce a detectable change in the seismic anisotropy pattern. Finally, as the strong annealing recorded by the microstructures did not significantly disperse the olivine CPO, it also did not erase the seismic anisotropy. The South Patagonian lithospheric mantle has thus a non-negligeable seimic anisotropy, which records the last deformation episode that affected this region.

Analysis of surface wave data for paths traversing the austral Andes and SE Patagonia highlight up to 5% polarization anisotropy with S_H faster than S_V waves in the shallow mantle lithosphere (Robertson Maurice et al., 2003). Below 60 km depth, S_H remains faster than S_V, but anisotropy is lower and seismic velocities are up to 5% slower than in the Preliminary Reference Earth Model (PREM). S_H faster than S_V implies subhorizontal lineations in the lithospheric mantle. The reported 5% of seismic anisotropy corresponds to the maximum anisotropy obtained for the average Pali Aike sample, and is close to the maximum anisotropy for the average Gobernador Gregores sample (Fig. 12). Yet these maximum polarization anisotropies would not be sampled by horizontally propagating waves if the foliation was horizontal (maximum values for this orientation will be lower: ~3–4%, Fig. 12).

Russo et al. (2010a,b) have detected an ENE polarization of the fast split teleseismic shear waves propagating in the vicinity of the present location of the Chile Triple Junction. These authors assumed that the olivine CPO producing this anisotropy is due to active asthenospheric mantle flow. However, we have shown that the lithospheric mantle xenoliths from Gobernador Gregores and Pali Aike do have a strong CPO. Moreover, to explain S_H faster than S_V lineations have to be subhorizontal in the lithospheric mantle and vertically propagating SKS will sample intermediate to strong S-wave birefringence (Fig. 12). This raises the question of the effect of lithospheric seismic anisotropy on splitting measurements. If both the lithospheric and asthenospheric lids are anisotropic, but have different CPO orientations, the fast split S-wave polarization direction and the delay time should vary with the backazimuth on the incoming waves. Such a variation is not described in Russo et al. (2010a,b). On the other hand, if the fabric in the lithosphere and the asthenosphere are similar, then delay times should be larger than those recorded since the thickness of the anisotropic layer traversed by a vertically propagating S wave would be large.

10. Conclusions

The medium- to coarse-granular or tabular textures, the low density of intracrystalline deformation features in olivine and pyroxenes and the common polygonal grain boundaries with 120° triple junctions suggest that all xenoliths from Gobernador Gregores and Pali Aike were affected by extensive annealing. However, all xenoliths show a well-developed olivine CPO and, for some of them, a pyroxene CPO that were acquired during a deformation episode predating annealing and which was not erased by it. The xenoliths of the two localities were also submitted to reactive melt percolation, evidenced by microstructural observations, modal compositions, and REE data. The relative timing between metasomatism and deformation was investigated through the comparison of olivine and pyroxene CPO data, where the lack of correlation between olivine and pyroxene CPO would imply post-deformation pyroxene addition through reactive melt percolation. However, correlation between olivine and pyroxene CPOs cannot be used to infer a pre- to synkinematic silica-enrichment, as it may also be accounted for by overgrowth of primary pyroxenes, which preserved their initial CPO. Late, post-kinematic reactive melt percolation is, in the other hand, clearly evidenced by the occurrence of undeformed amphibole and phlogopite and from the websteritic veins traversing the dunite from the Gobernador Gregores xenolith suite.

Analysis of the olivine CPO and low-angle misorientation data in the two xenolith suites implies deformation in the dislocation creep regime with preferential activation of [100]{0kl} system in olivine. Olivine CPO in Gobernador Gregores peridotites is essentially of [100]-fiber and orthorhombic types, whereas in Pali Aike [010]-fiber, fiber and orthorhombic olivine CPO types are equally represented. The association of [010]-fiber olivine CPO with microstructures with a tabular tendency suggests that the tabular olivine grains are probably produced by crystallographically controlled grain growth.

Seismic properties at room temperature conditions of average samples for each site are very homogeneous. The pattern of seismic velocities and anisotropies is very similar in the two localities, with the maximum splitting for S waves propagating in the foliation plane at high angle to the [100] axis concentration and the minimum splitting for S waves propagating at low angle to this direction, that is subparallel to the lineation. The larger proportion of peridotites with [010]-fiber fabric in Pali Aike relative to Gobernador Gregores does not seem to change this pattern. As neither the strong annealing recorded by the microstructures nor the modal metasomatism significantly dispersed the olivine CPO, they also did not erase the seismic anisotropy of the South Patagonian lithospheric mantle. This seismic anisotropy, which records the last major deformation episode that affected this region, should be taken into account in the interpretation of shear wave splitting data.

Acknowledgments

D. Mainprice is thanked for discussions and for providing softwares for analyzing/plotting CPO data and seismic properties. We also thank two anonymous reviewers whose corrections greatly improved an earlier version of the manuscript. C. Nevado and D. Delmas supplied high

Please cite this article as: Zaffarana, C., et al., Microstructures and seismic properties of south Patagonian mantle xenoliths (Gobernador Gregores and Pali Aike), Tectonophysics (2014), http://dx.doi.org/10.1016/j.tecto.2014.02.017

quality polished thin sections for EBSD measurements. CZ postdoctoral stay at Geosciences Montpellier was funded by a Bernard Houssay scholarship funded by the Ministère de l'Enseignement Supérieur et de la Recherche, France and the CONICET, Argentina. The research leading to these results was partially funded by the Ecos Sud project A09U01 "Evolution de la texture et de l'anisotropie lors de la déformation haute température des roches et des métaux". The EBSD-SEM national facility in Montpellier is supported by the Institut National de Sciences de l'Univers (INSU) du Centre National de la Recherche Scientifique (CNRS), France and by the Conseil Régional Languedoc-Roussillon, France.

References

Abramson, E.H., Brown, J.M., Slutsky, L.J., Zang, J., 1997. The elastic constants of San Carlos olivine to 17 GPa. J. Geophys. Res. 102, 12253–12263.

Aki, K., Christofferson, A., Husebye, E., 1977. Determination of the three-dimensional structure of the lithosphere. J. Geophys. Res. 82, 277–296.

Alexandrov, K.S., Ryzhova, T.V., 1961. Elastic properties of rock-forming minerals: layered silicates. Bulletin (Izvestiya) of the Academy of Sciences, USSR. Geophys. Ser. 6, 1799–1804.

Alexandrov, K.S., Belikov, B.P., Ryzhova, T.V., 1966. Calcul des constantes élastiques des roches d'après leur composition minéralogique. Nauk. SSSR, Serija Geologi eskaija URSS 2.

Aliani, P.A., Bjerg, E.A., Ntaflos, T., 2004. Evidencias de metasomatismo en el manto sublitosferico de Patagonia. Rev. Asoc. Geol. Argent. 59, 539–555.

Arndt, N.T., Guitreau, M., Boullier, A.-M., Le Roex, A., Tommasi, A., Cordier, P., Sobolev, A., 2010. Olivine, and the origin of kimberlite. J. Petrol. 51, 573–602.

Bachmann, F., Hielscher, R., Schaeben, H., 2010. Texture analysis with MTEX — free and open source software toolbox. Solid State Phenom. 160, 63–68.

Bachmann, F., Hielscher, R., Schaeben, H., 2011. Grain detection from 2d and 3d EBSD data — specification of the MTEX algorithm. Ultramicroscopy 111, 1720–1733.

Baptiste, V., Tommasi, A., Demouchy, S., 2012. Deformation and hydration of the lithospheric mantle beneath the Kaapvaal craton, South Africa. Lithos 149, 31–50.

Bascou, J., Tommasi, A., Mainprice, D., 2002. Plastic deformation and development of clinopyroxene lattice preferred orientations in eclogites. J. Struct. Geol. 24, 1357–1368.

Bascou, J., Delpech, G., Vauchez, A., Moine, B.N., Cottin, J.Y., Barruol, G., 2008. An integrated study of microstructural, geochemical, and seismic properties of the lithospheric mantle above the Kerguelen plume (Indian Ocean). Geochem. Geophys. Geosyst. 9, Q04036.

Ben Ismaïl, W., Mainprice, D., 1998. An olivine fabric database: an overview of upper mantle fabrics and seismic anisotropy. Tectonophysics 296, 145–157.

Bjerg, E.A., Ntaflos, T., Kurat, G., Dobosic, G., Labudía, C.H., 2005. The upper mantle beneath Patagonia, Argentina, documented by xenoliths from alkali basalts. J. S. Am. Earth Sci. 18, 125–145.

Breitsprecher, K., Thorkelson, D.J., 2009. Neogene kinematic history of Nazca–Antarctic–Phoenix slab windows beneath Patagonia and the Antarctic Peninsula. Tectonophysics 464, 10–20.

Brey, G.P., Köhler, T., 1990. Geothermobarometry in four-phase lherzolites II. New thermobarometers and practical assessment of existing thermobarometers. J. Petrol. 31, 1353–1378.

Bunge, H.J., 1982. Texture Analysis in Materials Sciences. Buttleworth, London.

Bystricky, M., Kunze, K., Burlini, L., Burg, J.P., 2000. High shear strain of olivine aggregates; rheological and seismic consequences. Science 290, 1564–1567.

Cande, S., Leslie, R., 1986. Late Cenozoic tectonics of the southern Chile trench. J. Geophys. Res. 91, 471–496.

Castro, A., Moreno-Ventas, I., Fernández, C., Vujovich, G., Gallastegui, G., Heredia, N., Martino, R.D., Becchio, R., Corretgé, L.G., Díaz-Alvarado, J., Such, P., García-Arias, M., Liu, D.Y., 2011. Petrology and SHRIMP U–Pb zircon geochronology of Cordilleran granitoids of the Bariloche area, Argentina. J. S. Am. Earth Sci. 32, 508–530.

Chai, M., Brown, J.M., Slutsky, L.J., 1997. The elastic constants of an aluminous orthopyroxene to 12.5 GPa. J. Geophys. Res. 102, 14779–14786.

Christensen, N.I., 1971. Fabric, seismic anisotropy and tectonic history of the Twin Sisters dunite. Geol. Soc. Am. Bull. 82, 1681–1694.

Collins, M.D., Brown, J.M., 1998. Elasticity of an upper mantle clinopyroxene. Phys. Chem. Miner. 26, 7–13.

Corbella, H., 1984. El volcanismo de la Altiplanicie del Somuncura. In: Ramos, V.A. (Ed.), Relatorio IX Congreso Geológico Argentino. San Carlos de Bariloche. Asociación Geológica Argentina, Buenos Aires, pp. 267–300.

Corbella, H., 2002. El campo volcano-tectónico de Pali Aike. In: Haller, M. (Ed.), Geología y Recursos Naturales de Santa Cruz. Asociación Geológica Argentina, Buenos Aires, pp. 285–302.

D'Orazio, M., Agostini, S., Mazzarini, F., Innocenti, F., Manetti, P., Haller, M.J., Lahsen, A., 2000. The Pali Aike Volcanic Field, Patagonia: slab-window magmatism near the tip of South America. Tectonophysics 321, 407–427.

Dalla Salda, L., Cingolani, C., Varela, R., 1992. Early Paleozoic orogenic belt of the Andes in southwestern South America: Result of Laurentia–Gondwana collision? Geology 20, 617–620.

Dantas, C., 2007. Caractérisation du manteau supérieur patagonien: les enclaves ultramafiques et mafiques dans les laves alcalines. (Ph.D. thesis) Université Toulouse III-Paul Sabatier, Toulouse 384.

Douglas, B.J., Saul, S.L., Stern, C.R., 1987. Rheology of the upper mantle beneath southernmost South America interred from peridotite xenoliths. J. Petrol. 95, 241–253.

Drury, M.R., Van Roermund, H.L.M., 1989. Fluid assisted recrystallization in upper mantle peridotite xenoliths from kimberlites. J. Petrol. 30, 133–152.

Duffy, T.S., Vaughan, M.T., 1988. Elasticity of enstatite and its relationship to crystal structure. J. Geophys. Res. 93, 383–391.

Dziewonski, A.M., Hager, B.H., O'Connell, R.J., 1977. Large scale heterogeneities in the lower mantle. J. Geophys. Res. 82, 239–255.

Falus, G., Tommasi, A., Ingrin, J., Csaba, S., 2008. Deformation and seismic anisotropy of the lithospheric mantle in the southeastern Carpathians: a mantle xenolith study. Earth Planet. Sci. Lett. 272, 50–64.

Frets, E., Tommasi, A., Garrido, C.J., Padrón-Navarta, J.A., Amri, I., Targuisti, K., 2012. Deformation processes and rheology of pyroxenites under lithospheric mantle conditions. J. Struct. Geol. 39, 138–157.

Gasparik, T., 1984. Two-pyroxene thermobarometry with new experimental data in the system CaO–MgO–Al_2O_3–SiO_2. Contrib. Mineral. Petrol. 87, 87–97.

Gorring, M.L., Kay, S.M., 2000. Carbonatite metasomatized peridotite xenoliths from southern Patagonia: implications for lithospheric processes and Neogene plateau magmatism. Contrib. Mineral. Petrol. 140, 55–72.

Gorring, M.L., Kay, S.M., 2001. Mantle processes and sources of Neogene slab window magmas from southern Patagonia, Argentina. J. Petrol. 42, 1067–1094.

Gorring, M.L., Kay, S.M., Zeitler, P.K., Ramos, V.A., Rubiolo, D., Fernandez, M.I., Panza, J.L., 1997. Neogene Patagonian plateau lavas: continental magmas associated with ridge collision at the Chile Triple Junction. Tectonics 16, 1–17.

Green, H.W., Radcliffe, S.V., 1972. Dislocation mechanisms in olivine and flow in the upper mantle. Earth Planet. Sci. Lett. 15, 239–247.

Green, D.H., Ringwood, A.E., 1967. The stability fields of aluminous pyroxene peridotite and garnet peridotite and their relevance in upper mantle structure. Earth Planet. Sci. Lett. 3, 151–160.

Green, D.H., Hibberson, W.O., Kovács, I., Rosenthal, A., 2010. Water and its influence on the lithosphere–asthenosphere boundary. Nature 467, 448–452.

Heintz, M., Debayle, E., Vauchez, A., 2005. Upper mantle structure of the South American continent and neighboring oceans from surface wave tomography. Tectonophysics 406, 115–139.

Herzberg, C., 1978. The bearing of phase equilibria in simple and complex systems on the origin and evolution of some well-documented garnet-websterites. Contrib. Mineral. Petrol. 66, 375–382.

Hess, H., 1964. Seismic anisotropy of uppermost mantle under oceans. Nature 203 (494), 629–631.

Hielscher, R., Schaeben, H., 2008. A novel pole figure inversion method: specification of the MTEX algorithm. J. Appl. Crystallogr. 41, 1024–1037.

Irving, A.J., 1974. Geochemical and high pressure experimental studies of garnet pyroxenite and pyroxene granulites xenoliths from the Delegate Basaltic Pipes, Australia. J. Petrol. 15 (1), 1–40.

Ivins, E.R., James, T.S., 1999. Simple models for late Holocene and present-day Patagonian glacier fluctuations and predictions of a geodetically detectable isostatic response. Geophys. J. Int. 138, 601–624.

Jung, H., Katayama, I., Jiang, Z., Hiraga, T., Karato, S., 2006. Effect of water and stress on the lattice-preferred orientation of olivine. Tectonophysics 421, 1–22.

Kay, S.M., Ramos, V.A., Marquez, M., 1993. Evidence in Cerro Pampa volcanic rocks for slab-melting prior to ridge-trench collision in Southern South America. J. Geol. 101, 703–714.

Kelemen, P.B., Hirth, G., Shimizu, N., Spiegelman, M., Dick, H.J., 1997. A review of melt migration processes in the adiabatically upwelling mantle beneath oceanic spreading ridges. Philosophical Transactions of the Royal Society of London. Series A: Mathematical. Phys. Eng. Sci. 355, 283–318.

Kempton, P.D., Lopez-Escobar, L., Hawkesworth, C.J., Pearson, D.G., Wright, D.W., Ware, A. J., 1999a. Spinel ± Garnet lherzolite xenoliths from Pali Aike, part 1: petrography, mineral chemistry and geothermobarometry. In: Gurney, J.J., Gurney, J.L., Pascoe, M.D., Richardson, S.H. (Eds.), Proceedings of Seventh International Kimberlite Conference. Red Roof Design, Cape Town, pp. 403–414.

Kempton, P.D., Hawkesworth, C.J., Lopez-Escobar, L., Pearson, D.G., Ware, A.J., 1999b. Spinel ± garnet lherzolite xenoliths from Pali Aike: part 2. Trace element and isotopic evidence bearing on the evolution of lithospheric mantle beneath southern Patagonia. In: Gurney, J.J., Gurney, J.L., Pascoe, M.D., Richardson, S.H. (Eds.), Proceedings of Seventh International Kimberlite Conference. Red Roof Design, Cape Town, pp. 415–428.

Klemme, S., 2004. The influence of Cr on the garnet–spinel transition in the Earth's mantle: experiments in the system MgO–Cr_2O_3–SiO_2 and thermodynamic modelling. Lithos 77, 639–646.

Klemme, S., O'Neill, H.S., 2000. The near-solidus transition from garnet lherzolite to spinel lherzolite. Contrib. Mineral. Petrol. 138, 237–248.

Kornprobst, J., 1970. Les péridotites et les pyroxénolites du massif ultrabasique des Beni Bouchera: une étude experimentale entre 1100 et 1500 °C, sous 15 à 30 kilobars de pression sèche. Contrib. Mineral. Petrol. 29, 290–309.

Lagabrielle, Y., Suárez, M., Rossello, E.A., Hérail, G., Martinod, J., Régnier, M., De la Cruz, R., 2004. Neogene to Quaternary tectonic evolution of the Patagonian Andes at the latitude of the Chile Triple Junction. Tectonophysics 385, 211–241.

Laurora, A., Mazzuccelli, M., Rivalenti, G., Vannucci, R., Zanetti, A., Barbieri, M.A., Cingolani, C.A., 2001. Metasomatism and melting in carbonated peridotite xenoliths from the mantle wedge: the Gobernador Gregores Case (Southern Patagonia). J. Petrol. 42, 69–87.

Lawrence, J.F., Wiens, D.A., 2004. Combined receiver-function and surface wave phase-velocity inversion using a niching genetic algorithm: application to Patagonia. Bull. Seismol. Soc. Am. 94, 977–987.

Please cite this article as: Zaffarana, C., et al., Microstructures and seismic properties of south Patagonian mantle xenoliths (Gobernador Gregores and Pali Aike), Tectonophysics (2014), http://dx.doi.org/10.1016/j.tecto.2014.02.017

Le Roux, V., Bodinier, J.L., Tommasi, A., Alard, O., Dautria, J.M., Vauchez, A., Riches, A.J.V., 2007. The lherz spinel lherzolite: refertilized rather than pristine mantle. Earth Planet. Sci. Lett. 259 (3–4), 599–612.
Linares, E., Gonzales, R.R., 1990. Catálogo de edades radimétricas de la República Argentina 1957–1987. Publ. Asoc. Geol. Argent. B 19, 628.
Mainprice, D., 1990. A Fortran program to calculate seismic anisotropy from the lattice preferred orientation of minerals. Comput. Geosci. 16, 385–396.
Mainprice, D., 2007. Seismic anisotropy of the deep earth from a mineral and rock physics perspective. Treatise Geophys. 437–491.
Mainprice, D., Humbert, M., 1994. Methods of calculating petrophysical properties from lattice preferred orientation data. Surv. Geophys. 15, 575–592.
Mainprice, D., Tommasi, A., Couvy, H., Cordier, P., Frost, D.J., 2005. Pressure sensitivity of olivine slip systems and seismic anisotropy of Earth's upper mantle. Nature 433, 731–733.
Mainprice, D., Hielscher, R., Schaeben, H., 2011. Calculating anisotropic physical properties from texture data using the MTEX open-source package. Geol. Soc. Lond., Spec. Publ. 360, 175–192.
Mazzarini, F., D'Orazio, M., 2003. Spatial distribution of cones and satellite-detected lineaments in the Pali Aike Volcanic Field (southernmost Patagonia): insights into the tectonic setting of a Neogene rift system. J. Volcanol. Geotherm. Res. 125, 291–305.
McDonough, W.F., Sun, S., 1995. The composition of the Earth. Chem. Geol. 120, 223–253.
Morgan, Z.T., Liang, Y., 2005. An experimental study of the kinetics of lherzolite reactive dissolution with applications to melt channel formation. Contrib. Mineral. Petrol. 150, 369–385.
Mpodozis, C., Ramos, V.A., 1989. The Andes of Chile and Argentina. In: Ericksen, G.E., Cañas Pinochet, M.T., Relnemund, J.A. (Eds.), Geology of the Andes and its Relation to Hydrocarbon and Mineral Resources. Circum-Pacific Council for Energy and Mineral Resources. TX Earth Science Series, Houston, pp. 59–90.
Mpodozis, C., Ramos, V.A., 2008. Tectónica Jurásica en Argentina y Chile: extensión, subducción oblícua, rifting, deriva y colisiones? Rev. Asoc. Geol. Argent. 63, 481–497.
Murdie, R.E., 1994. Seismicity and Neotectonics Associated with the Subduction of an Active Ocean Ridge-transform System in Southern Chile. University of Liverpool.
Murdie, R.E., Pugh, D.T., Styles, P., 1999. A lightweight, portable, digital probe for measuring the thermal gradient in shallow water sediments, with examples from Patagonia. Geo-Mar. Lett. 18, 315–320.
Murdie, R.E., Styles, P., Prior, D.J., Daniel, A.J., 2000. A new gravity map of southern Chile and its preliminary interpretation. Rev. Geol. Chile 27, 49–63.
Nicolas, A., Christensen, N.I., 1987. Formation of anisotropy in upper mantle peridotites—a review. In: Fuchs, K., Froideoaux, C. (Eds.), Composition, Structure and Dynamics of the Lithosphere–Asthenosphere System. Trans. ed. AGU, Washington, D.C., pp. 407–433 (16).
Nicolas, A., Boudier, F., Boullier, A.M., 1973. Mechanisms of flow in naturally and experimentally deformed peridotites. Am. J. Sci. 273, 853–876.
Niu, Y., Langmuir, C.H., Kinzler, R.J., 1997. The origin of abyssal peridotites: a new perspective. Earth Planet. Sci. Lett. 152, 251–265.
Obata, M., 1976. The solubility of Al_2O_3 in orthopyroxenes in spinel and plagioclase peridotites and spinel piroxenites. Am. Mineral. 61, 804–816.
Pankhurst, R.J., Rapela, C.W., 1995. Production of Jurassic rhyolite by anatexis in the lower crust of Patagonia. Earth Planet. Sci. Lett. 134, 23–36.
Pankhurst, R.J., Leat, P.T., Sruoga, P., Rapela, C.W., Marquez, M., Storey, B.C., Riley, T.R., 1998. The Chon Aike province of Patagonia and related rocks in West Antarctica: a silicic large igneous province. J. Volcanol. Geotherm. Res. 81, 113–136.
Pankhurst, R.J., Riley, T.R., Fanning, C.M., Kelley, S.P., 2000. Episodic silicic volcanism in Patagonia and the Antarctic Peninsula: chronology of magmatism associated with the break-up of Gondwana. J. Petrol. 41, 605–625.
Pankhurst, R.J., Rapela, C.W., Loske, W.P., Márquez, M., Fanning, C.M., 2003. Chronological study of the pre-Permian basement rocks of southern Patagonia. J. S. Am. Earth Sci. 16, 27–44.
Pankhurst, R.J., Rapela, C.W., Fanning, C.M., Márquez, M., 2006. Gondwanide continental collision and the origin of Patagonia. Earth-Sci. Rev. 76, 235–257.
Perkins III, D., Holland, T.J.B., Newton, R.C., 1981. The Al_2O_3 contents of enstatite in equilibrium with garnet in the system $MgO–Al_2O_3–SiO_2$ at 15–40 kbar and 900°–1,600 °C. Contrib. Mineral. Petrol. 78, 99–109.
Presnall, D., 1976. Alumina content of enstatite as a geobarometer for plagioclase and spinel lherzolites. Am. Mineral. 61, 582–588.
Ramos, V.A., 2008. Patagonia: a paleozoic continent adrift? J. S. Am. Earth Sci. 26, 235–251.
Ramos, V.A., Kay, S.M., 1992. The Southern Patagonian plateau basalts: retroarc testimony of a ridge collision, Argentina. Tectonophysics 205, 261–282.
Ramos, V.A., Kay, S.M., Singer, B., 2004. Las adakitas de la Cordillera Patagónica: Nuevas evidencias geoquímicas y geocronológicas. Rev. Asoc. Geol. Argent. 59, 693–706.
Rapela, C.W., Pankhurst, R.J., Fanning, C.M., Hervé, F., 2005. Pacific subduction coeval with the Karoo mantle plume: the Early Jurasssic Subcordilleran belt of northwestern Patagonia. Geol. Soc. Lond., Spec. Publ. 246, 217–239.
Ringwood, A.E., 1975. Composition and Petrology of the Earth's Mantle. New York.
Rivalenti, G., Mazzuccelli, M., Laurora, A., Ciuffi, S.I.A., Zanetti, A., Vannucci, R., Cingolani, C. A., 2004a. The backarc mantle lithosphere in Patagonia, South America. J. S. Am. Earth Sci. 17, 121–152.
Rivalenti, G., Zanetti, A., Mazzuchelli, M., Vannucci, R., Cingolani, C.A., 2004b. Equivocal carbonatite markers in the mantle xenoliths of the Patagonia backarc: the Gobernador Gregores case (Santa Cruz Province, Argentina). Contrib. Mineral. Petrol. 147, 647–670.
Robertson Maurice, S.D., Wiens, D.A., Koper, K.D., Vera, E., 2003. Crustal and upper mantle structure of southernmost South America inferred from regional waveform inversion. J. Geophys. Res. 108, 2038.
Russo, R.M., Gallego, A., Comte, D., Mocanu, V.I., Murdie, R.E., VanDecar, J.C., 2010a. Source-side shear wave splitting and upper mantle flow in the Chile Ridge subduction region. Geology 38, 707–710.
Russo, R.M., VanDecar, J.C., Comte, D., Mocanu, V.I., Gallego, A., Murdie, R.E., 2010b. Subduction of the Chile Ridge: upper mantle structure and flow. GSA Today 20, 4–10.
Schilling, M.E., Carlson, R.W., Conceição, R.V., Dantas, C., Bertotto, G.W., Koester, E., 2008. Re–Os isotope constraints on subcontinental lithospheric mantle evolution of southern South America. Earth Planet. Sci. Lett. 268, 89–101.
Skewes, M.A., Stern, C.R., 1979. Petrology and geochemistry of alkali basalts and ultramafic inclusions from the Pali-Aike volcanic field in Southern Chile and the origin of the Patagonian plateau lavas. J. Volcanol. Geotherm. Res. 6, 3–25.
Söllner, F., Miller, H., Hervé, M., 2000. An Early Cambrian granodiorite age from the pre-Andean basement of Tierra del Fuego (Chile): the missing link between South America and Antarctica? J. S. Am. Earth Sci. 13, 163–177.
Somoza, R., Ghidella, M.E., 2012. Late Cretaceous to recent plate motions in western South America revisited. Earth Planet. Sci. Lett. 331–332, 152–163.
Soustelle, V., Tommasi, A., Demouchy, S., Ionov, D., 2010. Deformation and fluid–rock interactions in the supra-subduction mantle: microstructures and water contents in peridotite xenoliths from the Avacha Volcano, Kamchatka. J. Petrol. 51, 363–394.
Stern, C.R., Futa, K., Saul, S., Skewes, M.A., 1986. Nature and evolution of the subcontinental mantle lithosphere below southern South America and implications for Andean magma genesis. Rev. Geol. Chile 27, 41–53.
Stern, C.R., Saul, S., Skewes, M.A., Futa, K., 1989. Garnet peridotite xenoliths from the Pali Aike basalts of southernmost South America. Kimberlites and Related Rocks, Geological Society of Australia, Carlton, Australia 735–744.
Stern, C.R., Frey, F.A., Futa, K., Kartman, R.E., Kyser, T.K., 1990. Trace-element and Sr, Nd, Pb and O isotopic compositions of Pliocene and Quaternary alkali basalts of the Patagonian Plateau lavas of southernmost South America. Contrib. Mineral. Petrol. 104, 294–308.
Stern, C.R., Kilian, R., Olker, B., Hauri, E.H., Kyser, T.K., 1999. Evidence from mantle xenoliths for relatively thin (<100 km) continental lithosphere below Phanerozoic crust of southernmost South America. Lithos 48, 217–235.
Tommasi, A., Tikoff, B., Vauchez, A., 1999. Upper mantle tectonics: three-dimensional deformation, olivine crystallographic fabrics and seismic properties. Earth Planet. Sci. Lett. 168, 173–186.
Tommasi, A., Mainprice, D., Canova, G., Chastel, Y., 2000. Viscoplastic self-consistent and equilibrium-based modeling of olivine lattice preferred orientations: implications for the upper mantle seismic anisotropy. J. Geophys. Res. Solid Earth 105, 7893–7908.
Tommasi, A., Vauchez, A., Ionov, D., 2008. Deformation, static recrystallization, and reactive melt transport in shallow subcontinental mantle xenoliths (Tok Cenozoic volcanic field, SE Siberia). Earth Planet. Sci. Lett. 272, 65–77.
Van Roermund, J., Boland, H., 1981. The dislocation substructures of naturally deformed omphacites. Tectonophysics 78, 403–418.
Vauchez, A., Dineur, F., Rudnick, R.L., 2005. Microstructure, texture and seismic anisotropy of the lithospheric mantle above a mantle plume. Insights from the Labait volcano xenoliths (Tanzania). Earth Planet. Sci. Lett. 232, 295–314.
Vollmer, F.W., 1990. An application of eigenvalue methods to structural domain analysis. Bull. Geol. Soc. Am. 102, 786–791.
Walter, M.J., Sisson, T.W., Presnall, D.C., 1995. A mass proportion method for calculating melting reactions and application to melting of model upper mantle lherzolite. Earth Planet. Sci. Lett. 135, 77–90.
Wenk, H.R., Bennett, K., Canova, G.R., Molinari, A., 1991. Modelling plastic deformation of peridotite with the self-consistent theory. J. Geophys. Res. B 96, 8337–8349.
Wood, B.J., Holloway, J.R., 1984. A thermodynamic model for sub-solidus equilibria in the system $CaO–MgO–Al_2O_3–SiO_2$. Geochim. Cosmochim. Acta 48, 159–176.
Zhang, S., Karato, S.-i, 1995. Lattice preferred orientation of olivine aggregates deformed in simple shear. Nature 375, 774–777.

Please cite this article as: Zaffarana, C., et al., Microstructures and seismic properties of south Patagonian mantle xenoliths (Gobernador Gregores and Pali Aike), Tectonophysics (2014), http://dx.doi.org/10.1016/j.tecto.2014.02.017